

# Radial Velocity

**Christophe Lovis**

Université de Genève

**Debra A. Fischer**

Yale University

The radial velocity technique was utilized to make the first exoplanet discoveries and continues to play a major role in the discovery and characterization of exoplanetary systems. In this chapter we describe how the technique works, and the current precision and limitations. We then review its major successes in the field of exoplanets. With more than 250 planet detections, it is the most prolific technique to date and has led to many milestone discoveries, such as hot Jupiters, multi-planet systems, transiting planets around bright stars, the planet-metallicity correlation, planets around M dwarfs and intermediate-mass stars, and recently, the emergence of a population of low-mass planets: ice giants and super-Earths. In the near future radial velocities are expected to systematically explore the domain of telluric and icy planets down to a few Earth masses close to the habitable zone of their parent star. They will also be used to provide the necessary follow-up observations of transiting candidates detected by space missions. Finally, we also note alternative radial velocity techniques that may play an important role in the future.

## 1. INTRODUCTION

Since the end of the XIXth century, radial velocities have been at the heart of many developments and advances in astrophysics. In 1888, Vogel at Potsdam used photography to demonstrate Christian Doppler's theory (in 1842) that stars in motion along our line of sight would exhibit a change in color. This color change, or wavelength shift, is commonly known as a Doppler shift and it has been a powerful tool over the past century, used to measure stellar kinematics, to determine orbital parameters for stellar binary systems, and to identify stellar pulsations. By 1953, radial velocities had been compiled for more than 15,000 stars in the General Catalogue of Stellar Radial Velocities (Wilson 1953) with a typical precision of  $750 \text{ m s}^{-1}$ , not the precision that is typically associated with planet-hunting. However, at that time, Otto Struve proposed that high precision stellar radial velocity work could be used to search for planets orbiting nearby stars. He made the remarkable assertion that Jupiter-like planets could reside as close as 0.02 AU from their host stars. Furthermore, he noted that if such close-in planets were ten times the mass of our Jupiter, the reflex stellar velocity for an edge-on orbit would be about  $2 \text{ km s}^{-1}$  and detectable with 1950's Doppler precision (Struve 1952).

Two decades later, Griffin & Griffin (1973) identified a key weakness in radial velocity techniques of the day; the stellar spectrum was measured with respect to an emission spectrum. However, the calibrating lamps (typically thorium argon) did not illuminate the slit and spectrometer collimator in the same way as the star. Griffin & Griffin outlined a strategy for improving Doppler precision to a remarkable  $10 \text{ m s}^{-1}$  by differentially measuring stellar line

shifts with respect to telluric lines. Assuming that telluric lines are at rest relative to the spectrometer, these absorption lines would trace the stellar light path and illuminate the optics in the same way and at the same time as the star. Although Griffin & Griffin did not obtain this high precision, they had highlighted some of the key challenges that current techniques have overcome.

By 1979, Gordon Walker and Bruce Campbell had a version of telluric lines in a bottle: a glass cell containing hydrogen fluoride that was inserted in the light path at the CFHT (Campbell & Walker 1979). Like telluric lines, the HF absorption lines were imprinted in the stellar spectrum and provided a precise wavelength solution spanning about  $50 \text{ \AA}$ . The spectrum was recorded with a photon-counting Reticon photodiode array. Working from 1980 to 1992, they monitored 17 main sequence stars and 4 subgiant stars and achieved the unprecedented precision of  $15 \text{ m s}^{-1}$ . Unfortunately, because of the small sample size, no planets were found. However, upper limits were set on  $M \sin i$  for orbital periods out to 15 years for the 21 stars that they observed (Walker et al. 1995).

Cross-correlation speedometers were also used to measure radial velocities relative to a physical template. In 1989, an object with  $M \sin i$  of  $11 M_{\text{Jup}}$  was discovered in an 84-day orbit around HD 114762 (Latham et al. 1989). The velocity amplitude of the star was  $600 \text{ m s}^{-1}$  and although the single measurement radial velocity precision was only about  $400 \text{ m s}^{-1}$ , hundreds of observations effectively beat down the noise to permit this first detection of a substellar object.

In 1993, the ELODIE spectrometer was commissioned on the 1.93-m telescope at Observatoire de Haute-Provence

(OHP, France). To bypass the problem of different light paths for stellar and reference lamp sources described by Griffin & Griffin (1973), two side-by-side fibers were used at ELODIE. Starlight passed through one fiber and light from a thorium argon lamp illuminated the second fiber. The calibration and stellar spectrum were offset in the cross-dispersion direction on the CCD detector and a velocity precision of about  $13 \text{ m s}^{-1}$  enabled the detection of a Jupiter-like planet orbiting 51 Pegasi (Mayor & Queloz 1995). In a parallel effort to achieve high Doppler precision, a glass cell containing iodine vapor was employed by Marcy & Butler (1995) to confirm the detection of a planetary companion around 51 Peg b. Both Doppler techniques have continued to show remarkable improvements in precision, and have ushered in an era of exoplanet discoveries.

## 2. DESCRIPTION OF THE TECHNIQUE

### 2.1. Radial Velocity Signature of Keplerian Motion

The aim of this section is to derive the radial velocity equation, i.e. the relation between the position of a body on its orbit and its radial velocity, in the case of Keplerian motion. We present here a related approach to Chapter 2 on Keplerian Dynamics. As shown there, the solutions of the gravitational two-body problem describe elliptical orbits around the common center of mass if the system is bound, with the center of mass located at a focus of the ellipses. Energy and angular momentum are constants of the motion. The semi-major axis of the first body orbit around the center of mass  $a_1$  is related to the semi-major axis of the relative orbit  $a$  through:

$$a_1 = \frac{m_2}{m_1 + m_2} a, \quad (1)$$

where  $m_1$  and  $m_2$  are the masses of the bodies.

In polar coordinates, the equation of the ellipse described by the first body around the center of mass reads:

$$r_1 = \frac{a_1(1 - e^2)}{1 + e \cos f} = \frac{m_2}{m_1 + m_2} \cdot \frac{a(1 - e^2)}{1 + e \cos f}, \quad (2)$$

where  $r_1$  is the distance of the first body from the center of mass,  $e$  is the eccentricity and  $f$  is the true anomaly, i.e. the angle between the periastron direction and the position on the orbit, as measured from the center of mass. The true anomaly as a function of time can be computed via Kepler's equation, which cannot be solved analytically, and therefore numerical methods have to be used (see Chapter 2).

In this section we want to obtain the relation between position on the orbit, given by  $f$ , and orbital velocity. More specifically, since our observable will be the radial velocity of the object, we have to project the orbital velocity onto the line of sight linking the observer to the system. In Cartesian coordinates, with the  $x$ -axis pointing in the periastron direction and the origin at the center of mass, the position and velocity vectors are given by:

$$\mathbf{r}_1 = \begin{pmatrix} r_1 \cos f \\ r_1 \sin f \end{pmatrix}, \quad (3)$$

$$\dot{\mathbf{r}}_1 = \begin{pmatrix} \dot{r}_1 \cos f - r_1 \dot{f} \sin f \\ \dot{r}_1 \sin f + r_1 \dot{f} \cos f \end{pmatrix}. \quad (4)$$

We now need to express  $\dot{r}_1$  and  $\dot{f}$  as a function of  $f$  in order to obtain the velocity as a function of  $f$  alone. In a first step, we differentiate Eq. 2 to obtain  $\dot{r}_1$ :

$$\dot{r}_1 = \frac{a_1 e (1 - e^2) \dot{f} \sin f}{(1 + e \cos f)^2} = \frac{e r_1^2 \dot{f} \sin f}{a_1 (1 - e^2)}. \quad (5)$$

Replacing  $\dot{r}_1$  in Eq. 4, we obtain after some algebra:

$$\dot{\mathbf{r}}_1 = \frac{r_1^2 \dot{f}}{a_1 (1 - e^2)} \begin{pmatrix} -\sin f \\ \cos f + e \end{pmatrix} \quad (6)$$

$$= \frac{h_1}{m_1 a_1 (1 - e^2)} \begin{pmatrix} -\sin f \\ \cos f + e \end{pmatrix}, \quad (7)$$

where  $h_1 = m_1 r_1^2 \dot{f}$  is the angular momentum of the first body, which is a constant of the motion. It can be expressed as a function of the ellipse parameters  $a$  and  $e$  as (see Chap. 2):

$$h_1 = \frac{m_2}{m_1 + m_2} h = \sqrt{\frac{G m_1^2 m_2^4 a (1 - e^2)}{(m_1 + m_2)^3}}. \quad (8)$$

Substituting  $h_1$  in Eq. 6, we finally obtain:

$$\dot{\mathbf{r}}_1 = \sqrt{\frac{G m_2^2}{m_1 + m_2} \frac{1}{a (1 - e^2)}} \begin{pmatrix} -\sin f \\ \cos f + e \end{pmatrix}. \quad (9)$$

As a final step, the velocity vector has to be projected onto the line of sight of the observer. We define the inclination angle  $i$  of the system as the angle between the orbital plane and the plane of the sky (i.e. the perpendicular to the line of sight). We further define the argument of periastron  $\omega$  as the angle between the line of nodes and the periastron direction (see Fig. 5 of Chapter 2 for an overview of the geometry). In a Cartesian coordinate system with  $x$ - and  $y$ -axes in the orbital plane as before and the  $z$ -axis perpendicular to them, the unit vector of the line of sight  $\mathbf{k}$  is given by:

$$\mathbf{k} = \begin{pmatrix} \sin \omega \sin i \\ \cos \omega \sin i \\ \cos i \end{pmatrix}. \quad (10)$$

The radial velocity equation is obtained by projecting the velocity vector on  $\mathbf{k}$ :

$$\begin{aligned} v_{r,1} &= \dot{\mathbf{r}}_1 \cdot \mathbf{k} \\ &= \sqrt{\frac{G}{(m_1 + m_2) a (1 - e^2)}} m_2 \sin i \\ &\quad \cdot (\cos(\omega + f) + e \cos \omega). \end{aligned} \quad (11)$$

This is the fundamental equation relating the radial velocity to the position on the orbit. From there we can derive the radial velocity semi-amplitude  $K = (v_{r,max} - v_{r,min})/2$ :

$$K_1 = \sqrt{\frac{G}{(1-e^2)}} m_2 \sin i (m_1 + m_2)^{-1/2} a^{-1/2}. \quad (12)$$

It is useful to express this formula in more practical units:

$$K_1 = \frac{28.4329 \text{ m s}^{-1}}{\sqrt{1-e^2}} \frac{m_2 \sin i}{M_{\text{Jup}}} \left( \frac{m_1 + m_2}{M_{\odot}} \right)^{-1/2} \left( \frac{a}{1 \text{ AU}} \right)^{-1/2}. \quad (13)$$

Alternatively, one can use Kepler's third law to replace the semi-major axis  $a$  with the orbital period  $P$ :

$$K_1 = \frac{28.4329 \text{ m s}^{-1}}{\sqrt{1-e^2}} \frac{m_2 \sin i}{M_{\text{Jup}}} \left( \frac{m_1 + m_2}{M_{\odot}} \right)^{-2/3} \left( \frac{P}{1 \text{ yr}} \right)^{-1/3}. \quad (14)$$

In the exoplanet case, only the radial velocity of the parent star is in general observable, because the planet-to-star flux ratio is so small ( $\lesssim 10^{-5}$ ). Radial velocity observations covering all orbital phases are able to measure the orbital period  $P$ , the eccentricity  $e$  and the RV semi-amplitude  $K_1$ . From these observables, the so-called 'minimum mass'  $m_2 \sin i$  can be computed, provided the total mass of the system  $m_1 + m_2$  is known. In practice, planetary masses are usually negligible compared to the mass of the parent star. The stellar mass can be obtained indirectly via spectroscopic analysis, photometry, parallax measurements and comparison with stellar evolutionary models. For bright, main-sequence FGKM stars, Hipparcos data and precise spectral synthesis make it possible to estimate stellar masses to  $\sim 5\%$ . Another, more precise way of obtaining stellar masses is via asteroseismic observations, since stellar pulsation frequencies are directly related to the basic stellar parameters such as mass, radius and chemical composition.

The unknown inclination angle  $i$  prevents us from measuring the true mass of the companion  $m_2$ . While this is an important limitation of the RV technique for individual systems, this fact does not have a large impact on statistical studies of exoplanet populations. Because inclination angles are randomly distributed in space, angles close to  $90^\circ$  (edge-on systems) are much more frequent than pole-on configurations. Indeed, the distribution function for  $i$  is given by  $f(i)di = \sin i di$ . As a consequence, the average value of  $\sin i$  is equal to  $\pi/4$  (0.79). Moreover, the a priori probability that  $\sin i$  is larger than 0.5 is 87%.

Eq. 13 gives RV semi-amplitudes as a function of orbital parameters. Table 2.1 lists a few typical examples for planets with different masses and semi-major axes orbiting a solar-mass star. As one can see, the search for exoplanets with the RV technique requires a precision of at least

Table 1: Radial velocity signals for different kinds of planets orbiting a solar-mass star.

Planet	$a$ (AU)	$K_1$ (m s $^{-1}$ )
Jupiter	0.1	89.8
Jupiter	1.0	28.4
Jupiter	5.0	12.7
Neptune	0.1	4.8
Neptune	1.0	1.5
Super-Earth ( $5 M_{\oplus}$ )	0.1	1.4
Super-Earth ( $5 M_{\oplus}$ )	1.0	0.45
Earth	0.1	0.28
Earth	1.0	0.09

$\sim 30 \text{ m s}^{-1}$  to detect giant planets. Towards lower masses, a precision of  $\sim 1 \text{ m s}^{-1}$  is necessary to access the domain of Neptune-like planets and super-Earths, while measurements at  $\sim 0.1 \text{ m s}^{-1}$  would be able to reveal the Earth. It is interesting to consider here planet searches around lower-mass stars, since the Doppler signal increases as  $1/\sqrt{m_1}$  at constant semi-major axis. For a  $0.1 M_{\odot}$  M dwarf, all RV amplitudes given in Table 2.1 must be multiplied by 3. Considering that the habitable zone around such stars may be as close as 0.1 AU, an Earth-like planet would induce a RV signal of  $0.9 \text{ m s}^{-1}$ . While the gain is significant compared to habitable Earths around FGK stars, it must be balanced by the intrinsic faintness of these stars, which makes it difficult to obtain high enough a signal-to-noise ratio to reach the required precision, even with 10-m telescopes.

## 2.2. Doppler Effect

The fundamental effect on which the radial velocity technique relies is the well-known Doppler effect. In flat spacetime (special relativity), an emitted photon of wavelength  $\lambda_0$  in the rest frame of the source will be detected at a different wavelength  $\lambda$  by an observer moving with respect to the emitter, where  $\lambda$  is given by (Einstein 1905):

$$\lambda = \lambda_0 \frac{1 + \frac{1}{c} \mathbf{k} \cdot \mathbf{v}}{\sqrt{1 - \frac{v^2}{c^2}}}. \quad (15)$$

In this equation,  $\mathbf{v}$  is the velocity of the source relative to the observer,  $\mathbf{k}$  is the unit vector pointing from the observer to the source in the rest frame of the observer, and  $c$  is the speed of light in vacuum. As one can see, the Doppler shift mainly depends on the projection of the velocity vector along the line of sight, i.e. the radial velocity of the source. There is also a dependence on the magnitude of the velocity vector, which means that the transverse velocity also contributes to the Doppler shift. However, this relativistic effect is often negligible in practical applications where velocities remain small compared to the speed of light.

In the framework of general relativity, the curvature of spacetime, giving rise to the so-called gravitational redshift, has to be taken into account in the derivation of the Doppler shift formula. Neglecting terms of order  $c^{-4}$  and higher, the

general-relativistic Doppler formula becomes, for an observer at zero gravitational potential (Lindgren & Dravins 2003):

$$\lambda = \lambda_0 \frac{1 + \frac{1}{c} \mathbf{k} \cdot \mathbf{v}}{1 - \frac{\Phi}{c^2} - \frac{v^2}{2c^2}}, \quad (16)$$

where  $\Phi$  is the Newtonian gravitational potential at the source ( $\Phi = GM/r$  at a distance  $r$  of a spherically-symmetric mass  $M$ ).

The Doppler effect, being a relation between wavelength (or frequency) of light and velocity of the emitter, opens the possibility to measure the (radial) velocity of a star as a function of time, thereby permitting the detection of orbiting companions according to the equations given in the previous section. In practice, the Doppler shift is measured on the numerous spectral lines that are present in stellar spectra. However, Earth-bound Doppler shift measurements must first be corrected from the effects of local motions of the observer, i.e. Earth rotation and revolution around the Sun, before they can be used to study the behaviour of the target star. The barycenter of the Solar System represents the most obvious local rest frame to which measurements should be referred. A corresponding suitable reference system centered on the Solar System barycenter, the International Celestial Reference System (ICRS), has been defined by the International Astronomical Union (IAU) and has become the standard reference system (Rickman 2001). Based on Eq. 16, the transformation of measured wavelengths at Earth to barycentric wavelengths is called 'barycentric correction' and is given by:

$$\lambda_B = \lambda_{\text{obs}} \frac{1 + \frac{1}{c} \mathbf{k} \cdot \mathbf{v}_{\text{obs}}}{1 - \frac{\Phi_{\text{obs}}}{c^2} - \frac{v_{\text{obs}}^2}{2c^2}}, \quad (17)$$

where  $\lambda_B$  is the wavelength that would be measured in the ICRS,  $\lambda_{\text{obs}}$  is the measured wavelength in the Earth-bound frame,  $\mathbf{k}$  is the unit vector pointing from the observer to the source in the ICRS,  $\mathbf{v}_{\text{obs}}$  is the velocity of the observer with respect to the ICRS, and  $\Phi_{\text{obs}}$  is the gravitational potential at the observer.

The main term in this equation is of course the projection of the observer velocity (in the ICRS) in the direction of the source at the time of the observation. It is made of two contributions: the Earth orbital velocity and the Earth rotational velocity at the observer's location. These can be computed using precise Solar System ephemerides such as those developed by JPL (Standish 1990) or IMCCE (Fienga et al. 2008). When aiming at radial velocity precisions of  $1 \text{ m s}^{-1}$  or below, all input parameters must be known to high precision and carefully checked. Target coordinates must be given in the ICRS, corrected from proper motions. The observatory clock must reliably give UT time, and ideally the photon-weighted mid-exposure time should be used. Finally, the observatory coordinates and altitude must be known precisely.

The relativistic term appearing in the denominator of Eq. 17 has a magnitude of a few  $\text{m s}^{-1}$  in velocity units and,

more importantly, exhibits variations at the level of only  $0.1 \text{ m s}^{-1}$  over the year due to the eccentricity of Earth's orbit. Therefore, if one is interested in radial velocity *variations* at a precision not exceeding  $0.1 \text{ m s}^{-1}$ , the relativistic term can be neglected and Eq. 17 reduces to the familiar classical expression

$$\lambda_B = \lambda_{\text{obs}} \left( 1 + \frac{1}{c} \mathbf{k} \cdot \mathbf{v}_{\text{obs}} \right). \quad (18)$$

After correcting the laboratory wavelength scale to the barycentric scale, the radial velocity of the source can finally be obtained from the expression

$$\lambda_B = \lambda_0 \frac{1 + \frac{1}{c} \mathbf{k} \cdot \mathbf{v}_*}{1 - \frac{\Phi_*}{c^2} - \frac{v_*^2}{2c^2}}, \quad (19)$$

where  $\mathbf{v}_*$  and  $\Phi_*$  are the source velocity and gravitational potential, respectively. Again, the relativistic term implies that it is in principle necessary to know the transverse velocity of the source to properly derive its radial velocity. However, if one is only interested in low-amplitude radial velocity *variations*, such as those produced by exoplanets, the relativistic term can also be dropped, yielding the familiar expression for the radial velocity:

$$\mathbf{k} \cdot \mathbf{v}_* = c \frac{\lambda_B - \lambda_0}{\lambda_0}. \quad (20)$$

We emphasize here that we are focusing on precise (i.e. reproducible), but not accurate (i.e. absolute), radial velocities. Indeed, obtaining absolute stellar radial velocities through the Doppler effect is a very difficult task due to many perturbing systematic effects, such as: gravitational redshift, convective blueshifts of stellar lines, line asymmetries, instrumental and wavelength calibration systematics, etc. These effects introduce unknown offsets on the measured radial velocities that may add up to  $\sim 1 \text{ km s}^{-1}$  for solar-type stars and high-resolution spectrographs. However, since they remain essentially constant with time, they do not prevent the detection of low-amplitude radial velocity signals. The reader is referred to Lindgren & Dravins (2003) for a stringent definition of the concept of radial velocity and an in-depth discussion of all relevant perturbing effects.

### 2.3. High-Resolution Spectra of Cool Stars

Stellar Doppler shift measurements rely on the presence of spectral features in the emergent spectrum. Since stars emit most of their electromagnetic energy between the UV and mid-IR domains, and since the UV and mid-IR domains themselves are not accessible from the ground, radial velocity work has always focused on spectral lines in the visible and near-IR regions. Stellar spectra vary widely across the different regions of the Hertzsprung-Russell diagram. Perhaps the single most relevant physical parameter that controls their general properties is the effective temperature of the stellar photosphere. On the hot side ( $T_{\text{eff}} \gtrsim 10,000 \text{ K}$ ), all chemical elements are at least partly

ionized and the atomic energy levels giving rise to electronic transitions in the visible and near-IR are depopulated (in other words, line opacities in these spectral regions become negligible). Since the spectrum is essentially a continuum, no Doppler shift measurements are possible on these stars. This fact is further reinforced by the usually high rotation rate of hot stars, which smears out spectral lines even more via rotational broadening. On the cool side of the HR diagram ( $T_{\text{eff}} \lesssim 3500$  K), spectral lines become increasingly densely packed, less contrasted and overlapping due to the presence of complex molecular bands. From an instrumental point of view, the intrinsic faintness of very cool stars makes it difficult to reach the required signal-to-noise ratio (SNR) for Doppler shift measurements. Moreover, such stars emit most of their flux in the IR, which puts more demanding constraints on ground-based instrumentation (cryogenic parts, background subtraction, removal of telluric lines, etc.).

Cool stars having spectral types from about F5 to M5 are therefore the best suited for precise radial velocity work. On the main sequence, this corresponds to masses between  $\sim 1.5$  and  $\sim 0.1 M_{\odot}$ , and this represents about the mass range over which the radial velocity technique has been able to find planetary companions. An exception to this rule is the red giant branch and clump region of the HR diagram, where more massive stars spend some time during their post-main sequence evolution. They are then sufficiently cool and slowly-rotating to be targeted by Doppler surveys (see Sect. 3.5).

Solar-type stars and M dwarfs exhibit thousands of absorption lines in their spectra, produced by all kinds of chemical elements. It is clear that one needs as many lines as possible to increase the radial velocity precision. However, strongly saturated stellar lines, such as hydrogen  $H\alpha$ , the calcium H & K lines or the Na D doublet should be avoided for high-precision radial velocity work because of their very broad wings and potentially variable chromospheric emission in their core. Looking more closely at the thousands of non-saturated lines present in the spectra of FGK stars, it clearly appears that Fe lines are by far the most numerous ones. Fe lines therefore represent the necessary basis for all precise Doppler shift measurements in these stars.

A key aspect of radial velocity work is to understand how the velocity precision depends on the shape of spectral lines. Intuitively, it is clear that precision will depend on three main parameters: the SNR in the continuum, the depth, and the width of the spectral line under consideration. The deeper and narrower the line, the better defined its centroid will be. Assuming approximately Gaussian shapes for spectral lines, it can indeed be shown that

$$\sigma_{\text{RV}} \sim \frac{\sqrt{\text{FWHM}}}{C \cdot \text{SNR}}, \quad (21)$$

where FWHM is the full width at half maximum of the line,  $C$  is its contrast (its depth divided by the continuum level), and SNR is the signal-to-noise ratio in the contin-

uum. From this formula it is clear that the broadening of spectral lines, caused either by stellar rotation or instrumental spectral resolution, can be a killer for radial velocity precision: an increase in rotational velocity, or decrease in resolution, simultaneously increases the FWHM and decreases the contrast since the total equivalent width must be conserved ( $C \sim 1/\text{FWHM}$ ). The RV precision therefore degrades with  $\text{FWHM}^{3/2}$ . As an example, the achievable RV precision between the Sun ( $v_{\text{rot}} = 2 \text{ km s}^{-1}$ ) and a young G2V star with  $v \sin i = 20 \text{ km s}^{-1}$  decreases by a factor  $\sim 32$ . Similarly, observing at a spectral resolution  $R = 100,000$  improves the precision by a factor 2.8 compared to the same observation at  $R = 50,000$ , provided the stellar lines are unresolved (this is the case for old solar-type stars) and the observations are made in the photon-limited regime.

More generally, in the presence of photon and detector noise, the Doppler information content of a stellar spectrum can be expressed by the formulae derived by Connes (1985) and Bouchy et al. (2001):

$$\sigma_{\text{RV},i} = c \frac{\sqrt{A_i + \sigma_D^2}}{\lambda_i \cdot |dA_i/d\lambda|}, \quad (22)$$

$$\sigma_{\text{RV}} = c \left( \sum_i \frac{\lambda_i^2 \cdot |dA_i/d\lambda|^2}{A_i + \sigma_D^2} \right)^{-1/2}. \quad (23)$$

In these equations,  $A_i$  is the flux in pixel  $i$  expressed in photoelectrons,  $\lambda_i$  is the wavelength of pixel  $i$  and  $\sigma_D$  is the detector noise per pixel, also expressed in photoelectrons.  $c$  is the speed of light in vacuum. In these formulae, the shape of spectral lines is hidden in the spectrum derivative  $dA_i/d\lambda$ . The steeper the spectrum, the higher the Doppler information content will be. Eqs. 22 and 23 must be used with some caution since they require the numerical computation of this spectrum derivative, which will be systematically overestimated at low SNR and in the continuum regions. As a result, the RV precision will tend to be overestimated as well.

As a practical example, we can now apply these formulae to the spectra of slowly-rotating solar-type stars, covering the whole visible range from 3800 to 7000 Å at a resolution  $R = 100,000$ . Typically, one obtains a global, photon-limited RV precision of  $1 \text{ m s}^{-1}$  when the SNR in the continuum at 5500 Å reaches  $\sim 145$ –180 per resolution element of 0.055 Å. The exact numbers depend on the projected rotational velocity of the star  $v \sin i$ , its metallicity and its spectral type, with K and M stars having more Doppler information in their spectra than G stars of a given magnitude (Bouchy et al. 2001). One therefore concludes that, as far as photon noise is concerned, the detection of exoplanets is within the capabilities of high-resolution echelle spectrographs on 1m-class telescopes and above.

As can be seen from Eqs. 21 and 23, the global Doppler information content depends both on the intrinsic line richness (density and depth) and on the SNR of the spectrum. Both parameters have to be taken into account to evaluate

the achievable RV precision on a particular type of stars observed with a particular instrument. In general, the spectral richness increases towards shorter wavelengths, and is particularly high in the blue visible region. As a consequence, the visible region is the natural choice for RV measurements of FGK stars, which also emit most of their light at these wavelengths. For M dwarfs, it is tempting to go to the near-IR. However, calculations on real spectra show that for early to mid-M dwarfs the higher flux in the near-IR does *not* compensate for the large amount of Doppler information in the visible. Only for late M dwarfs would a near-IR instrument be more efficient than a visible one. However, RV measurements in the near-IR have not reached yet the level of precision achieved by visible instruments. This may change in the near future.

## 2.4. Stellar Limitations to High-Precision Radial Velocities

Besides the general properties of spectra and spectral lines, other limitations on exoplanet detection around solar-type stars and M dwarfs have to be taken into account. Among these are several phenomena intrinsic to stellar atmospheres, which we will call ‘stellar noise’ or ‘astrophysical noise’ in the following. In this section we review the different sources of stellar noise, classified according to their typical timescales and starting on the high-frequency side.

### 2.4.1. P-mode oscillations

Stars having an outer convective envelope can stochastically excite p-mode oscillations at their surface through turbulent convection. These so-called solar-like oscillations have typical periods of a few minutes in solar-type stars and typical amplitudes per mode of a few tens of  $\text{cm s}^{-1}$  in radial velocity (e.g. Bouchy & Carrier 2001, Kjeldsen et al. 2005). The observed signal is the superposition of a large number of these modes, which may cause RV variations up to several  $\text{m s}^{-1}$ . P-modes characteristics vary from star to star. The oscillation frequencies scale with the square root of the mean stellar density, while the RV amplitudes scale with the luminosity-to-mass ratio  $L/M$  (Christensen-Dalsgaard 2004). As a consequence, oscillation periods become longer towards early-type stars along the main sequence, while they also increase when a star evolves off the main sequence towards the subgiant stage. Similarly, RV amplitudes become larger for early-type and evolved stars due to their higher  $L/M$  ratios. From the point of view of exoplanet search, low-mass, non-evolved stars are therefore easier targets because the stellar ‘noise’ due to p-modes is lower. However, even in the most favourable cases, it remains necessary to average out this signal if aiming at the highest RV precision. This can be done by integrating over more than 1-2 typical oscillation periods. Usually, an exposure time of 15 min is sufficient to decrease this source of noise well below  $1 \text{ m s}^{-1}$  for dwarf stars.

### 2.4.2. Granulation and supergranulation

Granulation is the photospheric signature of the large-scale convective motions in the outer layers of stars having a convective envelope. The granulation pattern is made of a large number of cells showing bright upflows and darker downflows, tracing the hot matter coming from deeper layers and the matter having cooled at the surface, respectively. On the Sun, the typical velocities of these convective motions are  $1\text{--}2 \text{ km s}^{-1}$  in the vertical direction. Fortunately for planet searches, the large number of granules on the visible stellar surface ( $\sim 10^6$ ) efficiently averages out these velocity fields. However, the remaining jitter due to granulation is expected to be at the  $\text{m s}^{-1}$  level for the Sun, probably less for K dwarfs (e.g. Pallé et al. 1995, Dravins 1990). The typical timescale for granulation, i.e. the typical time over which a given granule significantly evolves, is about 10 min for the Sun. On timescales of a few hours to about one day, other similar phenomena occur, called meso- and supergranulation. These are suspected to be larger convective structures in the stellar photosphere that may induce additional stellar noise, similar in amplitude to granulation itself. However, the origin and properties of these structures are still debated. Overall, granulation-related phenomena likely represent a significant noise source when aiming at sub- $\text{m s}^{-1}$  RV precision, and observing strategies to minimize their impact should be envisaged.

### 2.4.3. Magnetic activity

Magnetic fields at the surface of solar-type stars and M-dwarfs are responsible for a number of inhomogeneities in the stellar photosphere that represent yet another source of noise for planet searches via precise RV measurements (e.g. Saar & Donahue 1997, Santos et al. 2000, Wright 2005). Among these are cool spots and bright plages, which may cover a variable fraction of the stellar disk, evolve in time and are carried across the stellar disk by stellar rotation. Such structures affect RV measurements in several ways, but the most important effect comes from the flux deficit (or excess) in these regions, which moves from the blueshifted to the redshifted part of the stellar disk as the star rotates. This changes the shape of spectral lines and introduces modulations in the measured radial velocities on timescales comparable to the stellar rotation period. The properties of active regions vary widely from star to star depending on their mean activity level, which in turn mainly depends on stellar age for a given spectral type. Solar-type stars undergo a continuous decrease in rotational velocity as they age, starting with typical rotation periods of  $\sim 1\text{--}2$  days at 10 Myr, and slowing down to  $P_{\text{rot}} = 20\text{--}50$  days at 5 Gyr. Correspondingly, the magnetic dynamo significantly weakens with age and active regions become much smaller.

Generally speaking, stellar activity is a major problem for exoplanet searches around young stars ( $\lesssim 1$  Gyr), with dark spots causing RV variations larger than  $10\text{--}100 \text{ m s}^{-1}$ . Even hot Jupiters, causing RV amplitudes of hundreds of  $\text{m s}^{-1}$ , are expected to be difficult to detect around the

youngest stars (1–10 Myr) because stellar rotation periods are then close to the orbital periods. This may preclude investigations of planetary system formation with the RV technique at the stage where the protoplanetary disk is still present. A possible solution to activity-related problems in exoplanet searches is to observe in the near-IR domain, where the photospheric contrast of dark spots is lower than at visible wavelengths. However, this possibility remains to be explored. A broadly-used diagnostic of stellar activity is the line bisector, which traces line shape variations due e.g. to dark spots. In active stars, a clear anti-correlation is often seen between bisector velocity span and radial velocity, which, in certain cases, would make it possible to approximately correct the velocities for the influence of the spot (Queloz et al. 2001). The main problem with bisectors is that they lose most of their sensitivity in stars with a low projected rotational velocity  $v \sin i$ , because the rotation profile is not resolved any more (e.g. Desort et al. 2007).

The difficulties with young stars have led most planet-search surveys to effectively focus on old, slowly-rotating solar-type stars. These are usually much more quiet and a large fraction of them show activity levels sufficiently low to permit RV measurements at the  $1 \text{ m s}^{-1}$  level, and even below in favorable cases.

Detailed studies of the behavior of solar-type stars at this level of precision have yet to be done in order to understand the ultimate limitations of RV measurements set by stellar activity. For example, spectroscopic indicators can be used to monitor activity levels. The most famous one is the Ca II H&K chromospheric index which closely traces the presence of active regions (e.g. Wilson 1978, Baliunas et al. 1995). Precise measurements of this indicator and other spectroscopic diagnostics permits the derivation of stellar rotation periods even for older, chromospherically quiet stars. This analysis helps to distinguish between astrophysical noise sources and dynamical radial velocity signals. The general properties of activity-related noise in quiet stars have to be better quantified. Obviously, the Sun has been extensively studied in this respect and can serve as a prototype to understand other stars. However, solar research and instrumentation have usually pursued different scientific goals and therefore a direct comparison between solar and stellar observations is often not straightforward.

It is clear that the global characteristics of activity-related RV noise depend on at least four factors: the area covered by dark spots and plages, the stellar projected rotational velocity  $v \sin i$ , the stellar rotation period and the typical lifetime of active regions. While the first two factors directly influence the magnitude of the noise, the latter two determine its characteristic timescales and temporal behaviour. Dense sampling, averaging and binning of the data over timescales similar to the stellar rotation period may allow RV surveys to reach precisions as high as  $10 \text{ cm s}^{-1}$ , thus making it possible to detect Earth-like planets in the habitable zone around solar-type stars. Indeed, the power spectral density of stellar noise is expected to flat-

ten at frequencies lower than the rotation period, i.e. the noise is likely to become 'white' again, instead of 'red', when binning the data over sufficient periods of time. Since the timescale of stellar rotation ( $\sim 30$  days) is significantly smaller than the orbital periods of planets at 1 AU ( $\sim 300$  days), such a binning is indeed possible. Accumulating a large number of data points per stellar rotation cycle should then make it possible to efficiently average out stellar noise, although the ultimate attainable levels of precision remain controversial.

#### 2.4.4. Activity cycles

The Sun undergoes a well-known 11-year magnetic cycle, over which the number of active regions present on its surface dramatically changes. At solar minimum, there is sometimes no spot at all to be seen during several months, while at activity maximum about 0.2% of the solar surface may be covered with spots. This obviously impacts the achievable RV precision, although the lack of solar RV data obtained with the 'stellar' technique makes it difficult to quantitatively estimate the minimal and maximal RV variability. Other solar-type stars also exhibit similar activity cycles, as shown by Ca II H&K measurements. One can therefore suspect that the RV jitter of solar-type stars varies in time with the activity cycle. Besides varying short-term *scatter* in the radial velocities, there may also be *systematic trends* due to the varying average fraction of the photosphere covered with spots. Such effects may arise, for example, from changes in the granulation pattern that take place in active regions: solar observations show that granular motions tend to freeze due to strong magnetic fields in these regions. As a result, spectral lines may show reduced (or even vanishing) convective blueshifts, and therefore induce a systematic RV shift in the disk-integrated spectrum (Saar & Fischer 2000, Lindegren & Dravins 2003). However, such effects remain to be better explored and quantified among Doppler planet-search survey stars.

On the other hand, about 10–20% of old solar-type stars seem to be in a very quiet state, having a low mean activity level and showing no cyclic variations. Part of these stars may be in a so-called Maunder-minimum state, as the Sun in the XVIIth century. Such stars represent ideal targets for high-precision RV exoplanet searches. Ongoing Doppler surveys have been accumulating a sufficient number of Ca II H&K measurements to be able to identify this low-activity population in the solar neighbourhood, and RV campaigns focusing on these stars are likely to push stellar RV noise down to unprecedented levels. High-quality, densely-sampled RV datasets obtained on such stars will eventually answer the questions about the ultimate limits set by stellar activity on the RV technique.

## 2.5. Instrumental Challenges to High-Precision Radial Velocities

Measuring Doppler shifts with a precision of  $1 \text{ m s}^{-1}$  is a truly challenging task from an instrumental point of view.

Indeed, this corresponds to the measurement of wavelength shifts of a few  $10^{-5}$  Å, which, for a  $R = 100,000$  high-resolution instrument, represent  $\sim 1/3000$  of the line width or about  $1/1000$  of a CCD pixel on the detector. In practice, this normally cannot be achieved on a single spectral line because of insufficient SNR. Only the use of thousands of lines in stellar *and* wavelength calibration spectra makes it possible to reach such high levels of precision. These numbers, along with those concerning photon noise (Sect. 2.3), make it obvious that high spectral resolution ( $R \gtrsim 50,000$ ), large spectral coverage and high efficiency are necessary instrumental prerequisites to achieve radial velocity measurements at the  $\text{m s}^{-1}$  level. This explains why high-resolution, cross-dispersed echelle spectrographs have been systematically chosen for this purpose.

In practice, the problem is that a variety of instrumental effects can potentially cause instrumental shifts 2–3 orders of magnitude larger than the required precision of  $1 \text{ m s}^{-1}$ . The main effects are described below.

#### 2.5.1. Variations in the index of refraction of air

Changes in ambient temperature and pressure in the spectrograph translate into wavelength shifts due to the varying index of refraction of air. These shifts may amount to several hundreds of  $\text{m s}^{-1}$  during a single night. Indeed, a temperature change of 0.01 K or a pressure change of 0.01 mbar are sufficient to induce a drift of  $1 \text{ m s}^{-1}$ . These large-amplitude drifts must therefore be measured and/or corrected for to high accuracy.

#### 2.5.2. Thermal and mechanical effects

Temperature variations of mechanical and optical parts in the spectrograph induce mechanical flexures and optical effects (e.g. PSF changes) that mimic wavelength shifts on the detector. Similarly, moving parts and changes in instrumental configuration may also induce such drifts. Depending on instrumental design and ambient conditions, these effects may easily reach several tens to hundreds of  $\text{m s}^{-1}$ .

#### 2.5.3. Slit illumination

A spectrograph is basically an optical device producing a dispersed image of the entrance slit on the detector. Therefore, any variations in the slit illumination will translate into variations in the recorded spectrum, including PSF changes and shifts in the main-dispersion direction, i.e. wavelength shifts. Illumination variations arise from changing observing conditions (seeing, airmass), telescope focus, telescope guiding, possible vignetting along the light path, etc. As an order-of-magnitude calculation, a small photocenter shift of  $1/100$  of the slit width, due for example to guiding corrections, will induce a  $30 \text{ m s}^{-1}$  radial velocity shift in a  $R = 100,000$  spectrograph. This shows how critical slit illumination is for high-precision radial velocities. Two philosophies have been developed to overcome this major difficulty: a self-referencing method which superimposes iodine lines on the stellar spectrum (see Sect. 2.6), and the use

of optical fibers to feed the spectrograph, taking advantage of their high light-scrambling properties (see Sect. 2.7).

#### 2.5.4. Wavelength calibration

The stellar spectrum must be precisely wavelength-calibrated using a stable, well-characterized reference having a large number of spectral lines extending over the largest possible wavelength range. We briefly discuss here the intrinsic properties of different calibration sources, and defer the description of how they are used to Sects. 2.6 and 2.7. Long-term wavelength stability of spectral lines at the level of  $1 \text{ m s}^{-1}$  ( $\sim 10^{-9}$  in relative units) is not a trivial requirement and it is necessary to carefully examine all relevant physical effects that may affect the spectrum of calibration systems at this level of precision.

The two main calibration sources used for high-precision RV measurements have been iodine cells and ThAr hollow-cathode lamps. Molecular iodine vapor provides a dense forest of absorption features between 5000 and 6200 Å, while ThAr lamps produce thousands of emission lines over the whole visible and near-IR ranges. Iodine cells are in widespread use in different areas of physics where they serve as absolute wavelength calibrators. In high-precision radial velocity work, they have demonstrated a long-term stability at the  $\sim 1\text{--}2 \text{ m s}^{-1}$  level. However, their intrinsic limitations have to be clarified. Slight short-term or long-term variations in iodine pressure may affect the overall shape of the complex iodine spectrum, made of numerous, Doppler-broadened and overlapping molecular transitions. Moreover, the usable wavelength range is limited to  $\sim 1000$  Å, which makes it impossible to use the stellar Doppler information in other spectral regions. Finally, the Doppler information content of the iodine itself is a function of the achieved SNR in the continuum, which is determined by the stellar flux in the case of star+iodine exposures (see Sect. 2.6). As a consequence, high-SNR observations are required. This sets strong constraints on the target magnitude and/or exposure time.

On the other hand, ThAr lamps also have their advantages and drawbacks. They have also demonstrated a long-term stability at the  $\sim 1\text{--}2 \text{ m s}^{-1}$  level and cover a larger spectral range than iodine. Their spectra show, however, numerous blends and a large dynamic range in line intensities which complicate the precise measurement of line positions. They also have a limited lifetime. Aging effects induce changes in line intensities and small wavelength shifts probably due to slow pressure variations in the lamps. Argon is most sensitive to these effects and Ar lines may drift by several tens of  $\text{m s}^{-1}$  over the lifetime of a lamp. It is therefore important to avoid using these lines in the wavelength calibration process. Th lines are much less sensitive, but drifts of a few  $\text{m s}^{-1}$  have nonetheless been measured. These can be corrected to high precision by measuring the differential drift of Ar lines with respect to Th lines, knowing the sensitivity ratio between them. With this procedure ThAr lamps have demonstrated a long-term and lamp-to-



lamp stability at the  $\sim 30 \text{ cm s}^{-1}$  level (Lovis et al. 2010, in preparation).

In the near-IR domain, finding an appropriate calibrator is even more difficult. ThAr lamps may be used, but in most cases they do not provide a high enough density of lines for a precise calibration. Gas cells with various molecules have been proposed but none of them appears to meet all the requirements such as sufficient wavelength coverage, high line density and depth, non-superposition with telluric lines, usability, etc. A straightforward solution is to use the numerous telluric lines available in the near-IR as wavelength references. However, great care has to be taken in disentangling stellar and telluric lines. And, more importantly, telluric lines are known to be variable at the level of  $\sim 5\text{--}10 \text{ m s}^{-1}$  due to atmospheric winds and airmass effects.

Clearly, the ideal calibration source for high-precision RV measurements remains to be invented. A promising new approach is the development of the laser comb technology for use in astronomy (Murphy et al. 2007). Laser frequency combs deliver an extremely regular pattern of equally-spaced emission lines (in frequency) over a potentially broad wavelength range. Their decisive advantage comes from the fact that line wavelengths can be precisely controlled by locking the comb to an atomic clock, creating a direct link between the most accurate frequency references ever developed and optical frequencies. The accuracy and stability of comb lines is then basically given by the accuracy of the atomic clock, which can easily exceed  $10^{-11}$  in relative units (corresponding to less than  $1 \text{ cm s}^{-1}$ ). While such systems will definitively solve the reliability problems encountered with other calibration sources, they still have to be adapted to high-resolution astronomical spectrographs. The main difficulty is that current laser repetition rates ( $\sim 1 \text{ GHz}$ ) are too low by a factor of  $\sim 10$  for the resolution of astronomical spectrographs. In other words, consecutive comb peaks are much too close to each other even at  $R = 100,000$  resolution. A possible solution to this problem is to filter out unwanted modes using a Fabry-Pérot cavity (Li et al. 2008, Steinmetz et al. 2008, Braje et al. 2008). In this way, only 1 out of 10 modes, for example, can be transmitted, producing a clean comb spectrum for the spectrograph. Stringent constraints apply to the filtering cavity, however, which should not jeopardize the intrinsic comb accuracy by introducing instabilities or imperfections in the filtering. Another difficulty of laser frequency combs, especially in the visible domain, is the need for a broad wavelength coverage. In brief, these systems have not yet reached a level of reliability and practicality that would make them routinely usable at astronomical observatories. The rapid development of this technology should nevertheless lead to satisfactory solutions to these problems in the near future, making laser combs the calibrator of choice for ultra-high-precision radial velocity measurements.

#### 2.5.5. Detector-related effects

CCD detectors have a number of imperfections that may also impact radial velocity precision. First of all, CCD pixels do not all have the same sensitivity, due partly to intrinsic sensitivity variations and partly to variations in physical size. Flat-fielding cannot make the difference between both effects. Variations in pixel-to-pixel size have an impact on the wavelength solution and may cause spurious small-scale shifts when the stellar spectrum moves on the detector. A promising way to calibrate pixel properties would be to use a tunable wavelength reference, such as a laser frequency comb, that would be able to scan the CCD pixels and measure their response and size.

Thermal stability and control of the detector are also important since thermal dilation and contraction directly affect the dispersion solution. These effects can be corrected with both methods presented in Sects. 2.6 and 2.7.

Another potentially damaging effect is the charge transfer efficiency (CTE) of the CCD. During CCD readout, charges are transferred from pixel to pixel towards the readout ports, whereby a small fraction of the total charge is inevitably left behind at each step. As a result, line profiles are slightly asymmetrized, producing an apparent shift of spectral lines. Typical fractional losses of modern CCDs are around  $\sim 10^{-6}$  per transfer. Normally, this is just low enough to induce shifts that remain small or comparable to the photon noise on line positions. However, some CCDs seem to be of poorer quality, and in particular a significant degradation of CTE as a function of signal level has been noticed in several cases. This means that at lower signal-to-noise ratios, CTE becomes so low as to induce line shifts which clearly exceed random noise, i.e. systematic effects as a function of SNR are produced. Great care should therefore be taken in selecting and characterizing CCD devices for high-precision radial velocity instruments. If the CTE behaviour as a function of flux can be adequately calibrated, CTE-induced effects could in principle be corrected, but it is obviously better to choose a high-quality chip in the first place.

#### 2.5.6. Spectrum contamination

All features appearing in a spectrum which are not related to the target star may induce spurious radial velocity signals. Telluric lines from Earth's atmosphere represent one such example, with a particularly high density of absorption bands in the red and the near-IR. Contaminated spectral regions must be either rejected or properly treated since they are at rest in the observer's frame, contrary to stellar lines. Consequently, the main result of pollution by telluric lines will be a spurious one-year periodic signal in the radial velocities caused by Earth's motion around the Sun. The visible region is much less affected by telluric lines than the near-IR, but several zones starting at  $\sim 5500 \text{ \AA}$  should nonetheless be avoided.

Another important contamination source is moonlight. Diffuse moonlight pollutes the sky background with the re-

flected solar spectrum, which is superimposed onto the target star spectrum. This obviously also induces spurious radial velocity signals. Their magnitude depends on the relative brightness of the sky with respect to the source in the entrance slit of the spectrograph. Sky transparency is thus an important factor in this respect. Observations close to the Moon or in poor weather conditions when the Moon is present should be avoided.

Finally, the target spectrum may also be contaminated by the light of faint companions or background objects located sufficiently close on the sky to also enter the spectrograph slit. Obvious contaminations due to binary components of similar magnitude are usually easy to identify in the spectrum itself or in the radial velocities (large variations). This is not the case for faint contaminants with magnitude differences larger than  $\sim 5$  mag. Such objects may induce subtle radial velocity variations both on the short- and long-term. Short-term effects arise from the varying relative mixture of target and contaminant lights due to seeing and telescope pointing. On longer timescales, binary stars in the background may induce RV variations with the period of the binary that could mimic a planetary signal. In most cases, a careful monitoring of line shape variations, e.g. using bisector diagnostics, is able to reveal the presence of contaminants.

## 2.6. The Iodine Cell Technique

As noted in Sect. 2.5, velocity measurements of  $1 \text{ m s}^{-1}$  correspond to Doppler wavelength shifts,  $d\lambda$ , of order 1/1000th of a pixel shift. One technique for measuring such tiny shifts makes use of a glass cell containing iodine, which imposes a rich forest of molecular absorption lines into the stellar spectrum. The iodine lines serve as a grid against which the almost imperceptible stellar line shifts can be measured. The molecular transitions span a wavelength range from 5000 Å to 6200 Å. For long-term stability, it is critical that the column density of the reference gas remain constant over the length of the observing program, which may span decades, so once the iodine is in place, the cell is permanently sealed.

An iodine cell can easily be constructed in a chemistry lab. The glass cell is constructed by a glass blower with a small side tube welded onto the cylindrical body of the cell (part of a manifold for importing the iodine gas) and optical flats welded at both ends of the glass cylinder. After construction, anti-reflective coatings can be applied to the flat surfaces to minimize light losses. The cell should be cleaned with an acidic solution and thoroughly rinsed with water. The cell is then placed in a drying oven for a few hours to ensure that the interior is completely dry. Otherwise, trapped water vapor can condense in the cold night air at the telescope, fogging the inside surface of the exposed optical flats. Once dry, a grain of solid iodine is inserted into the manifold and the system is sealed and pumped to low pressure with a hi-vac pump. The entire cell and manifold are then placed into a water bath at a temperature of 37 C

to sublime the iodine, which fills the cell with a lavender-pink gas. With the I<sub>2</sub> gas now at constant vapor pressure, the glass blower permanently seals off the side tube. The trace amount of iodine is quite non-reactive with glass and the cell has a stable quantity of molecular I<sub>2</sub> that will condense into a solid spec if the temperature of the cell is lower than 37 C.

For use at an observatory, a thermocouple is taped to the side of the iodine cell and the cell is wrapped with heat tape. A temperature controller maintains a constant temperature of 55C throughout the night to ensure that all of the enclosed iodine is in a gaseous state at a constant vapor pressure. The iodine cell is inserted in the light path, ideally in front of the slit because it is a heat source. If that is not possible, then the system needs to be thermally isolated to prevent convective currents and temperature variations in the spectrometer. The optical surfaces of the I<sub>2</sub> cell and the I<sub>2</sub> gas opacity result in about 15% light loss.

In contrast to the well-separated and deep HF molecular lines, the I<sub>2</sub> absorption lines are dense and narrow. Fig. 2.6 (left) shows just a 2 Å wavelength segment of the Iodine spectrum obtained with a Fourier Transform Spectrometer (FTS) obtained with a resolution of about 900,000 (Blake 2008). Fig. 2.6 (right) shows the spectrum of that same I<sub>2</sub> cell, illuminated with a rapidly rotating (featureless) B type star and observed at Lick Observatory with the Hamilton spectrometer ( $R=55,000$ ). The quality of the spectrum is degraded by the lower spectral resolution and by the point spread function (PSF) of the instrument. However, using the FTS spectrum as a starting point, it is possible to find a PSF model, which, when convolved with the FTS spectrum (left) will produce the observed spectrum (right). This is a key step in modeling program observations (i.e., stellar observations made with the iodine cell).

Doppler analysis with an iodine reference cell is carried out by forward modeling, rather than cross correlation. The first step is to model an observation of the iodine spectrum (Fig. 2.6, right). It is good practice to obtain an iodine spectrum at the beginning and end of each night to obtain initial guesses for the wavelength solution and the PSF model. A rapidly rotating B-type star is an excellent light source for the iodine spectrum. The stellar spectrum is essentially featureless and the light illuminates the optics in the same manner as the program observations. Because the PSF varies spatially over the detector, the spectrum is divided into smaller chunks, typically 2 or 3 Å wide and a wavelength solution and PSF model is derived for each of these chunks. A Levenberg-Marquardt algorithm drives the model fit for each chunk. To create the model, the matching segment is extracted from the FTS iodine spectrum (containing the wavelength information), then splined onto the oversampled wavelength scale of the observation and convolved with a PSF description.

Valenti et al. (1995) describe a flexible technique for modeling the PSF as a sum of Gaussians. A central Gaussian accommodates most of the PSF, but several (five or more) Gaussians are also placed at fixed offsets from the

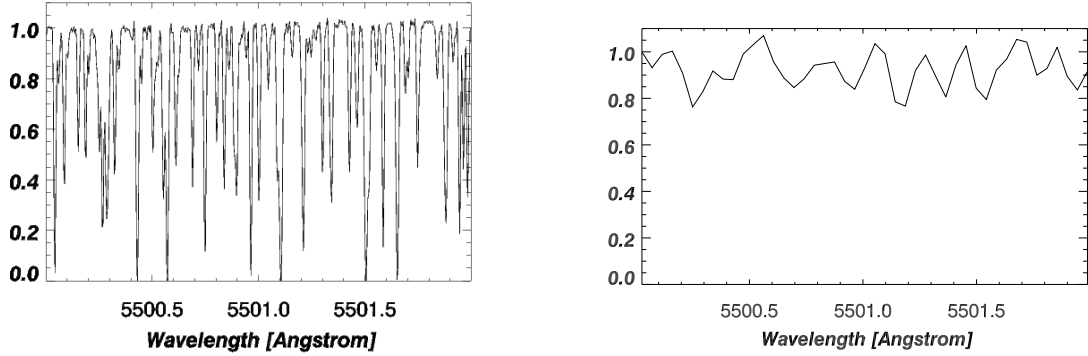


Fig. 1.— Left: an  $R=900,000$  FTS scan of the molecular iodine gas cell spanning only  $2 \text{ \AA}$ . Right: a spectrum of the same cell, illuminated by light from a rapidly rotating B type star and observed with the Hamilton spectrometer at  $R=55,000$ . The iodine lines contain both wavelength and PSF information.

central Gaussian. These flanking Gaussians are allowed to piston in amplitude to model asymmetries in the wings of the PSF. In this first step of modeling an iodine spectrum, there is no Doppler shift to fit, so the free parameters in the Levenberg-Marquardt fitting algorithm consist of the wavelength of the first pixel in the chunk, the dispersion across the chunk, and the PSF parameters (i.e., the FWHM of the central PSF Gaussian and the amplitudes of the flanking Gaussians).

The next step is to model the program observations: stellar observations taken with the iodine cell. The previous analysis of the iodine spectrum provides initial guesses for both the wavelength solution and the PSF model that should be used for the stellar observations and the Doppler shift of the star,  $d\lambda = \lambda v/c$ , is the important additional free parameter. In order to carry out the forward modeling of program observations, three ingredients are needed to model the program observations: the FTS iodine spectrum, a PSF model, and an intrinsic stellar spectrum (ISS).

Ideally, the ISS would have extremely high resolution and high signal-to-noise. In practice, the ISS is generally obtained with the same spectrometer as the program star observations. The starting point for the ISS is a so-called template observation, an observation of the star made without the iodine cell and with higher signal-to-noise and higher spectral resolution. Because the template spectrum is smeared by the spectrometer PSF, a deconvolution is carried out to try to recover the true ISS. Observations of featureless B stars through the iodine cell are taken before and after template observations and the PSFs that are recovered from modeling the iodine spectra are used in the deconvolution algorithm. To the extent that the deconvolution fails or introduces ringing in the continuum because of noise, the ISS is less than perfect and compromises Doppler precision.

To model the program observations, the deconvolved

stellar template  $S(\lambda)$  (our best representation for the true ISS) is multiplied by the FTS iodine spectrum  $I_2(\lambda+d\lambda)$  and convolved with the PSF description:

$$[S(\lambda) \cdot I_2(\lambda + d\lambda)] \otimes PSF = I_{obs}(\lambda) . \quad (24)$$

The free parameters for each chunk of the program observations include the all-important wavelength shift (which gives the velocity of the star), the wavelength of the first pixel, dispersion across the chunk, continuum normalization and the parameters used to describe the PSF. Fig. 2.6 shows the template observation (left) and the program observation (right) containing iodine absorption lines. The overplotted red dots represent the synthetic model created with Eq. 24.

With about 80 pixels and 15 free parameters, typical model fits yield a reduced  $\chi^2$  for each chunk of about 1.0. Individual chunks typically contain a few spectral lines and provide velocities that are accurate to  $30\text{--}50 \text{ m s}^{-1}$ . The relative change in velocity is always made with respect to the same wavelength segment; barycentric velocities change the location of spectral lines on the physical format, so the chunks vary in pixel space, but are always the same size and contain the same stellar lines. The spectral chunks are independent measurements of the velocity; the uncertainty or precision of the Doppler measurement is the standard deviation of the velocities for all of the chunks and improve over the single chunk precision by the square root of the number of chunks. The velocity for a particular observation is the mean velocity difference in all of the chunks.

The most significant weakness in Doppler modeling is uncertainty in the PSF model. The PSF model is critical to both the deconvolution of the template spectrum and the best-fit model of the program observations. While physical constraints can be included to model the wavelength solution (it should be continuous from chunk to chunk and con-

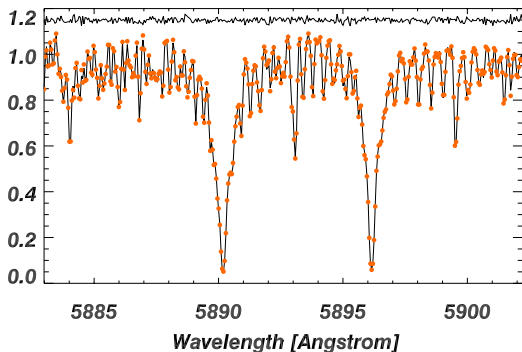


Fig. 2.— A template observation is obtained without the iodine cell (left) and deconvolved with a PSF model then used to model the program observation of that star (right). The synthetic model is overplotted with red dots on the program observation that contains many narrow iodine absorption lines.

tinuous over the order) and the dispersion (it should also be a smooth function of wavelength across the order and stable throughout the night), the PSF is more problematic. If the PSF only consisted of an instrumental component, then it would vary slowly over the night or season with changing temperature or pressure in the spectrometer. However, the uncontrolled component of the PSF is the variable slit image. Changes in seeing or errors in telescope guiding produce spatial and temporal changes in the cone of light that enters the spectrometer. Because the optical elements in the spectrometer are illuminated differently from observation to observation, the PSF changes from one observation to the next. A fiber optic cable would scramble the light at the slit and overcome this source of error. With a more stable PSF, it would be possible to simultaneously solve for the PSF of a given spectral chunk in stacks of several observations taken during a given night. This would provide a more robust PSF for template deconvolution (to produce the ISS) and a more accurate PSF description for Doppler analysis of program observations.

## 2.7. The Simultaneous Reference Technique

Another method to achieve high-precision RV measurements without self-referencing the stellar spectra is to build a dedicated instrument in which all possible sources of RV errors are minimized or corrected to high precision. This is the philosophy of the so-called “simultaneous reference” technique, or ThAr technique (Baranne et al. 1996). Going through the different instrumental effects listed in Sect. 2.5, it appears that the three most important problems to deal with are the variations in the index of refraction of air, mechanical flexures and slit illumination. The first two are internal effects in the spectrograph. To track and correct them, the basic idea is to inject a second, reference spectrum into

the spectrograph *simultaneously* with the scientific observation. Normally, a ThAr lamp is used for this purpose. The instrument has therefore two channels: a science and a simultaneous-reference channel. Before scientific observations (at the beginning of the night), wavelength calibration exposures are acquired by injecting the ThAr spectrum into *both* channels. This gives independent dispersion solutions for both channels. Obviously, these wavelength calibrations are only strictly valid at the moment they are taken. The idea is to use the simultaneous-reference channel to monitor instrumental drifts during the night and to correct the wavelength calibration accordingly. The underlying assumption is that the above-mentioned effects (varying index of refraction and mechanical flexures) will perturb the dispersion solutions of both channels in the same way, because both channels follow very similar paths in the spectrograph, from the slit to the detector. The instrumental drift is measured by comparing, in the simultaneous-reference channel, the ThAr spectrum obtained at the beginning of the night to the ThAr spectrum obtained simultaneously with the stellar observation. The measured drift is then subtracted on the science channel, assuming it suffered the same instrumental variations.

The long-term precision of this technique relies on the wavelength calibration obtained at the beginning of each night in the science channel. The derived dispersion solution must be as precise as possible since it determines the “baseline” wavelength calibration for each night. The position of ThAr emission lines must be properly measured, taking care of the blending between neighboring lines and weighting the lines according to their individual Doppler information content. Individual laboratory wavelengths have to be precise enough to avoid introducing excess scatter around dispersion solutions compared to photon noise. To this purpose, an updated list of ThAr reference wavelengths has been published recently (Lovis & Pepe 2007).

Slit illumination is the third major source of instrumental radial velocity jitter. RV shifts induced by atmospheric turbulence and telescope guiding cannot be corrected with the simultaneous-reference channel. In this case, the only way to proceed is to minimize as much as possible illumination variations, i.e. to scramble the light as much as possible before injecting it into the spectrograph, and to stabilize telescope guiding. This is achieved by using optical fibers to link the telescope to the spectrograph, and by developing a high-accuracy guiding system. Optical fibers reduce the inhomogeneities in the light distribution by a factor of typically  $\sim 500$ . Moreover, optical systems exchanging near-field and far-field (‘double scramblers’) can be used to further homogenize the light beam. With all these precautions, it has been possible to reduce illumination jitter down to the equivalent of  $\sim 10^{-4}$  of the slit width, corresponding to an RV jitter of  $\sim 0.3 \text{ m s}^{-1}$  for a  $R = 100,000$  spectrograph. Further improvements are certainly possible.

The result of this whole strategy is a precisely wavelength-calibrated stellar spectrum, on which the radial velocity can now be measured. This is done with a variant of the cross-

correlation method. Cross-correlation is an efficient way of computing the global shift between two similar signals. In this case, we would need a reference spectrum for each target star, against which we would correlate the observed spectrum. However, this would require a very large observational effort, since thousands of very high-SNR spectra are needed. A much simpler strategy is to use a binary 'mask' containing 'holes' at the rest wavelength of stellar lines, i.e. a binary transmission function with 1's at the position of stellar lines and 0's elsewhere. Cross-correlating the stellar spectrum with such a mask yields a kind of average stellar 'master' line made of the piling up of all lines transmitted through the mask. This procedure is optimal in the sense that it extracts the whole Doppler information from the spectrum using a noise-free template and concentrates it into a single cross-correlation function (CCF). Actually, to really optimize signal extraction, stellar lines have to be weighted by their relative contrast, since Doppler information is proportional to line depth (see Eq. 21 and Pepe et al. 2002). Since, for a given star, all lines used in the mask can be assumed to have the same FWHM, line depth is the only relevant parameter to include in the optimal weights (SNR is included by construction). In principle, it would be possible to develop a binary mask for each spectral type. However, differences between close spectral types are not significant from the point of view of signal extraction and experience has shown that a single mask for each main type (G, K, M) is usually sufficient. Finally, the radial velocity is measured by fitting a suitable model to the CCF, usually a Gaussian for slowly-rotating stars. In the whole procedure, the important point is to always use the same mask, model and correlation parameters for a given star, to avoid introducing 'algorithm noise' in the radial velocities.

The simultaneous-reference technique has been successfully used since 1993 and the development of the ELODIE spectrograph at Observatoire de Haute-Provence (OHP, France), which led to the discovery of the first exoplanet around a normal star (Mayor & Queloz 1995). From about  $10 \text{ m s}^{-1}$  in the early days, the precision of the technique has been continuously improved since then, triggered by further instrumental developments such as CORALIE (Queloz et al. 2000) at La Silla Observatory (Chile), SOPHIE at OHP (Bouchy et al. 2006), and particularly HARPS, also at La Silla (Mayor et al. 2003). All these instruments are cross-dispersed echelle spectrographs covering the whole visible range. ELODIE and CORALIE have spectral resolutions  $R = 50,000$  and  $60,000$  respectively, and are installed in a separate room isolated from the telescope. They are exposed to changing ambient pressure and temperature. Consequently, the typical nightly drifts measured in the simultaneous-reference channel amount to  $\sim 100 \text{ m s}^{-1}$ . SOPHIE (the successor of ELODIE) has  $R = 75,000$  and lies in a temperature- and pressure-stabilized enclosure, which reduces nightly drifts to a few  $\text{m s}^{-1}$ . As far as performances are concerned, ELODIE was able to reach a precision of  $\sim 7 \text{ m s}^{-1}$ , while CORALIE has achieved  $3\text{--}5 \text{ m s}^{-1}$  and SOPHIE  $\sim 3 \text{ m s}^{-1}$ . The three in-

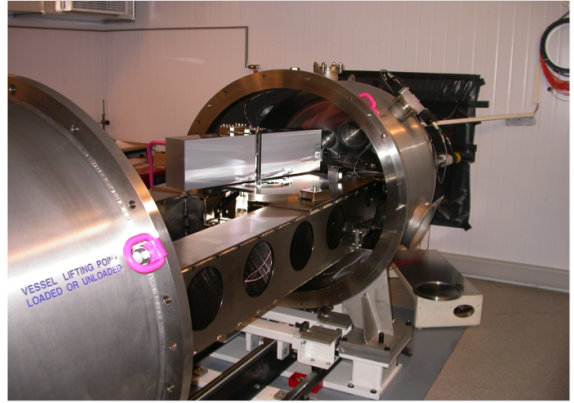


Fig. 3.— The HARPS spectrograph installed on the ESO 3.6m-telescope at La Silla Observatory, Chile. In this picture the vacuum vessel is open and the echelle grating is visible on the optical bench.

struments have been monitoring more than 2000 stars in the solar neighborhood. They have been very successful in discovering exoplanets, with more than 100 giant planets detected and many transiting candidates confirmed. Many statistical properties of the exoplanet population could be derived from these large surveys (see e.g. Udry & Santos 2007).

In 2003, the installation of HARPS (High Accuracy Radial velocity Planet Searcher) on the European Southern Observatory 3.6m telescope at La Silla marked a further major improvement in radial velocity precision. HARPS was designed from the beginning to minimize all instrumental RV errors, with the goal of achieving  $1 \text{ m s}^{-1}$ . Most importantly, it is installed in a temperature-controlled enclosure, the spectrograph itself being in a vacuum vessel (see Fig. 2.7). Temperature is kept constant throughout the year to  $\pm 0.01 \text{ K}$  and pressure is maintained below  $0.01 \text{ mbar}$ . As a consequence, nightly drifts as measured in the simultaneous-reference channel never exceed  $1 \text{ m s}^{-1}$ . Spectral resolution is  $R = 115,000$ , which, coupled to the larger telescope aperture, gives a significant gain in radial velocity precision as far as photon noise is concerned. Thanks to all these improvements, HARPS has achieved an unprecedented long-term precision of  $\sim 50 \text{ cm s}^{-1}$ , and even  $\sim 20 \text{ cm s}^{-1}$  on the short term (within a night). These performances have created new scientific possibilities: the search for Neptune-like planets and super-Earths down to a few Earth masses (e.g. Lovis et al. 2006, Mayor et al. 2009a). Indeed, these objects induce radial velocity signals smaller than  $3\text{--}4 \text{ m s}^{-1}$  and were therefore extremely difficult to detect with previous instruments. In a few years of operations, HARPS has revolutionized our knowledge of low-mass planets and will be able to deliver reliable statistics on this new population in the coming years (see Sects. 3.6 and 3.7).

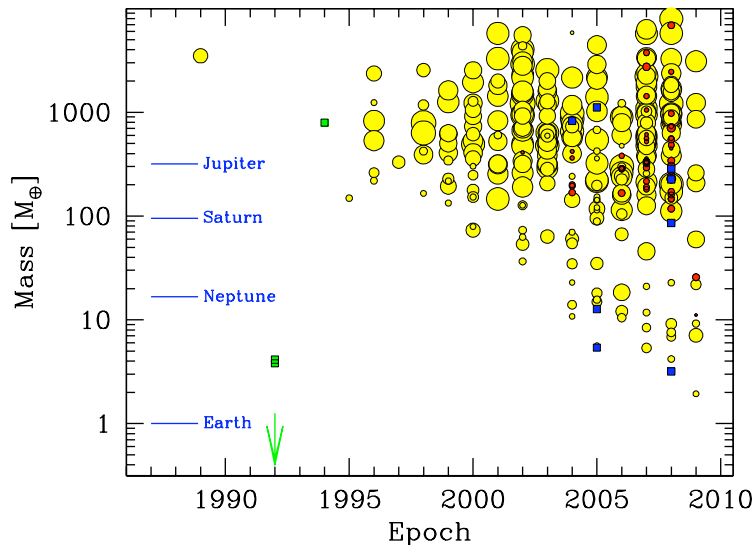


Fig. 4.— Timeline of exoplanet detections in a mass vs. year of discovery diagram. Symbol sizes are proportional to orbital eccentricity. The continuously decreasing detection threshold illustrates the progress of radial velocity surveys and shows that planet searches have now entered the Earth-mass domain.

### 3. MILESTONE DISCOVERIES AND HIGHLIGHTS

#### 3.1. Overview: 15 Years of Discoveries

Fig. 3.1 gives an overview of exoplanet discoveries as a function of time, from 1989 to 2009. The plot shows just how fast this new field of astronomy has developed in recent years and become one of the hot topics of the moment. At the forefront of this breakthrough stands the radial velocity technique, which has detected the majority of the known exoplanets. Individual major discoveries and milestones are discussed in the following sections.

#### 3.2. 51 Peg: the First Exoplanet Orbiting a Solar-Type Star, and the First Hot Jupiter

As mentioned in the Introduction, major instrumental efforts were being made in the 1980's and the early 1990's to improve radial velocity precision in the hope of finding extrasolar giant planets and brown dwarfs around nearby solar-type stars. Campbell et al. (1988) obtained precise ( $\sim 10 \text{ m s}^{-1}$ ) RV measurements of about 20 nearby stars using a hydrogen-fluoride cell as a wavelength reference. Shortly afterwards, Latham et al. (1989) announced the discovery of an object with a minimum mass of  $11 M_{\text{Jup}}$  around the solar-type star HD 114762. Because the unknown inclination angle of the system could only make this object heavier than the deuterium burning limit, it was considered as a brown dwarf or even a very low-mass star. In 1992, the search for low-mass companions saw an unexpected development: the discovery of three Earth-mass

objects orbiting the millisecond pulsar PSR 1257+12 using the pulsar timing technique (Wolszczan & Frail 1992, see Chapter 8 on Pulsar Planets). Although this demonstrated that planetary bodies may exist in widely diverse environments, the detected objects likely evolved in a different manner than Solar System planets.

Finally, new RV surveys of solar-like stars using the two main techniques described in Sects. 2.6 and 2.7 (Butler et al. 1996, Baranne et al. 1996) started to produce their first results. The achieved precisions of  $5\text{--}10 \text{ m s}^{-1}$  were adequate to easily detect Jupiter-mass planets on close orbits. However, the existence of such objects was not anticipated and observing strategies were really designed to find Solar System analogs, i.e. gas giants at  $5\text{--}10 \text{ AU}$ . It came therefore as a huge surprise when Mayor & Queloz (1995) announced the discovery of an object with a minimum mass of  $0.5 M_{\text{Jup}}$  orbiting the star 51 Peg in only 4.23 days. The detection was made with the ELODIE spectrograph at Observatoire de Haute-Provence (France), where a survey of  $\sim 150$  nearby stars was being carried out. The original radial velocity curve is shown in Fig. 3.2. It first had to be demonstrated that the signal indeed was dynamical, and was not related to spurious instrumental or stellar surface phenomena. The confirmation of the reality of the signal had to wait only a few weeks until Marcy & Butler (1995) published their own data on 51 Peg. Within one year, this team announced two more distant giant planets (Marcy & Butler 1996, Butler & Marcy 1996) and three other close-in



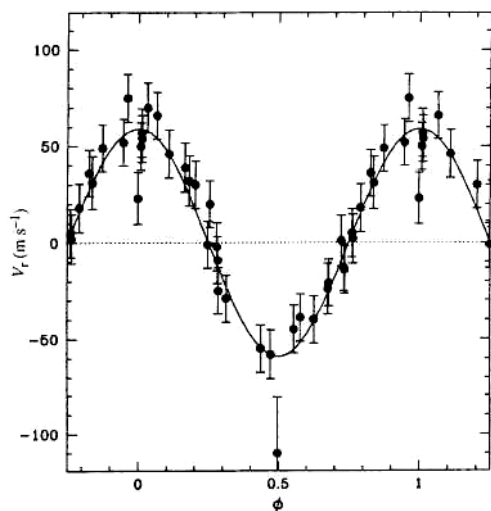


Fig. 5.— Original radial velocity curve of the star 51 Peg, phased to a period of 4.23 days, obtained with the ELODIE spectrograph (Mayor & Queloz 1995). The signal is caused by an orbiting companion with a minimum mass of  $0.47 M_{\text{Jup}}$ , revealing for the first time an exoplanet around another solar-type star.

51 Peg-like planets (Butler et al. 1997). These discoveries marked the beginning of the highly successful search for planets using precise radial velocities. Moreover, a new category of planets, unknown in our Solar System emerged: the hot Jupiters.

Planet formation theories did not foresee the existence of such exotic objects, for the simple reason that it is impossible to form them so close to their parent star. Protoplanetary disks do not contain enough material, hydrogen in particular, in their hot inner regions to possibly form any gas giant. It was thus necessary to invoke a new physical mechanism to explain the existence of hot Jupiters: inward migration of giant planets formed beyond the ice line, caused by interactions with the protoplanetary disk. Migration has remained a major topic of research since then, involving complex physical processes which are not completely understood yet (see Chapter 14 on Planet Migration).

### 3.3. Ups And: the first Multi-Planet System

One of the first detected hot Jupiter planets orbits the F8V star Upsilon Andromedae (Butler et al. 1997). The first 36 Doppler measurements from Lick Observatory for Upsilon Andromedae spanned 9 years and revealed a planet in a 4.617 day orbit with a mass of about  $0.7 M_{\text{Jup}}$ . The data also showed residual velocity variations with a period of about 2 years and velocity amplitude of about  $50 \text{ m s}^{-1}$ . However, announcement of a second planet seemed premature in 1997. After 53 additional measurements from Lick Observatory, spanning two more years, it was clear by eye that this second planet suspected by Butler et al. (1997) had

good phase coverage. The Advanced Fiber Optic Echelle (AFOE) was also being used to carefully monitor this star and in 1999, the Lick and AFOE data were combined for a joint solution. Surprisingly, the double-planet model failed to yield a reasonable  $\chi^2$  statistic.

There are many ways to fit multiple planet systems, however all require a reasonable initial guess for the orbital parameters. In the early days of Keplerian modeling we modeled the systems sequentially with a Levenberg-Marquardt algorithm, first fitting and then subtracting theoretical velocities for the dominant system and then checking for periodicities in the residual velocities. This sequential process was possible for a couple of reasons:

1. Kepler's Laws dictate that the orbital period of the planet is primarily a function of semi-major axis, and the necessary condition of gravitational stability planets. Therefore, the signals from gas giant planets in a multi-planet system will generally be well separated in frequency (i.e., the inverse orbital period).
2. For most planetary systems with gas giant planets, there was typically one dominant planet with a large amplitude and relatively short-period Doppler signal.

In the case of Upsilon Andromedae, the short period system was modeled in a high-cadence subset of the data that spanned a few months. The  $75 \text{ m s}^{-1}$  signal from the 4.617-day planet was modulated by a long period Doppler signal with similar velocity amplitude. Because the fit to the double planet system was inadequate (with a poor  $\chi^2$  statistic), the theoretical double-planet velocities were subtracted from the data and the residual noise showed a nearly sinusoidal variation, suggesting the presence of a third planet. This incredible result appeared in the Lick and AFOE data and the independent confirmation was critical for this first detection of a multi-planet system. The velocities for this triple planetary system continue to march along the predicted theoretical curve. Fig. 3.3 shows the latest velocities after subtracting the 4.617-day planet (for clarity).

The challenge of modeling multi-planet systems is greater when the planets are in resonant orbits and orbital periods are commensurate or when velocity amplitudes are smaller (lower signal-to-noise). For multi-planet systems with low mass (rocky) planets, the highest Doppler precision is required to identify all components in the system. In all multi-planet systems, there are non-Keplerian perturbations from gravitational interactions between planets that can result in slow modifications to a simpler superposition of Keplerian models.

### 3.4. Transiting Planets discovered with Radial Velocities

After the detection of the first exoplanets with the Doppler technique, there was skepticism by some astronomers regarding the true nature of these objects. Because the Doppler technique only measures line-of-sight velocity, the orbital inclination is unresolved and  $M \sin i$ ,

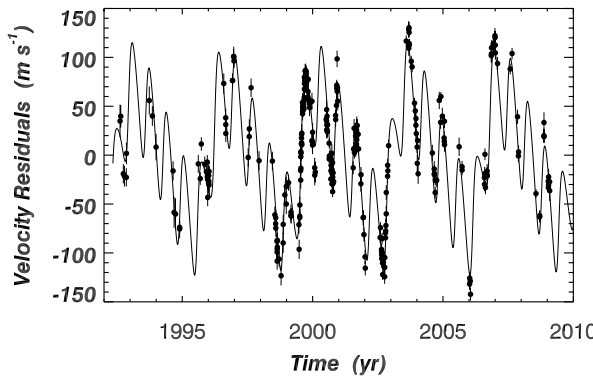


Fig. 6.— Radial velocity time series of the Ups And system spanning almost 20 years. The solid line shows the best-fit multi-Keplerian model. The signal of the closest planet Ups And b has been subtracted for clarity.

not  $M$  (mass) is actually measured. For small inclinations (nearly face-on orbits) the true mass of the object could even be stellar.

[ An exercise for the student: calculate the integrated probability that some of the detected exoplanets are actually stellar binaries in face-on orbits. First, calculate the threshold inclination that would push  $M \sin i$  to  $70 M_{\text{Jup}}$  (the stellar mass threshold) for the ensemble of known exoplanets. Then, calculate the statistical probability of observing an inclination between zero and the threshold inclination:  $P = 1 - \cos i_{\text{thresh}}$ . Summing all these probabilities yields a statistical estimate of the number of exoplanets with inclinations likely to move them to stellar masses. ]

While the Doppler technique cannot resolve the orbital inclination, it can determine other orbital parameters and predict the time of transit if the inclination is close to 90 degrees (edge-on). Planets are more likely to transit if they are close to the star (see chapter on transits). The probability that a close hot Jupiter will transit is relatively large ( $\sim 10\%$ ); therefore, photometric follow-up is carried out for all of the short-period planets. By 1999, ten hot Jupiters had been detected with Doppler observations and none of these exoplanets seemed to transit their host stars. The eleventh hot Jupiter, HD 209458b, finally produced the characteristic dimming expected from a transiting planet at exactly the time predicted with radial velocity data. Two independent groups made the Doppler detection with photometric follow-up (Charbonneau et al. 2000, Henry et al. 2000) that definitively confirmed the interpretation of radial velocity wobbles as exoplanets.

[ An exercise for the student: calculate the integrated

probability that transiting planets exist in the ensemble of known exoplanets. For a transiting planet,  $\sin i_{\text{transit}}$  must be greater than the ratio of the stellar diameter to the semi-major axis of the orbit (or use the periastron distance). Calculate the probability for this transit inclination for each system. Summing all of these probabilities yields a statistical estimate of the number of Doppler-detected exoplanets with transit-favorable inclinations. ]

While most transiting exoplanets are now detected with photometric surveys, a few important transiting planets were first detected in Doppler programs and can be given the whimsical designation of "Troppler" planets. Important examples include HD 209458 and HD 189733, which are further discussed in the chapter on planetary atmospheres.

HD 149026b (Sato et al. 2005) was detected as part of the N2K search for hot Jupiters orbiting metal-rich stars. This star exhibited confusing radial velocities that were difficult to model initially; in retrospect, it was because four of the first seven radial velocities were serendipitously obtained during transit. Because of the Rossiter-McLaughlin effect (see the corresponding chapter), the velocities deviated from Keplerian motion. HD 149026b has a mass that is 10% greater than Saturn and a radius 10% smaller than Saturn. Subsequent models showed that the planet must therefore contain a heavy element core of about  $70 M_{\oplus}$ , more akin to a super-Neptune than a hot Jupiter. Because the photometric decrement during transit was only 0.003 magnitudes, this would have been a challenging detection for photometric surveys of the day; the initial Doppler detection was key to demonstrating an unexpected range in the interior structure of gas giant planets.

Doppler observations detected a planet orbiting GJ 436, an M2.5V star (Butler et al. 2004). Subsequent photometric observations at the putative transit ephemeris times showed that the planet orbiting this M dwarf star was transiting (Gillon et al. 2007). The orbital period of this planet is just 2.64 days and the planet mass is just 22 times that of the Earth. The photometric transit depth of 0.009 magnitudes is larger than HD 149026b because of the smaller radius of the host star. This "Troppler" planet remains one of the most intriguing transiting planets because it is the first detected hot Neptune and because it orbits a low mass M dwarf star.

The photometric transit probability is greatest for short-period planets, which hug the host star. However, the Doppler technique has been unique in identifying two transiting planets with orbital periods longer than 10 days. Both of these planets are in eccentric orbits and are therefore part time hot Jupiters during periastron passage. HD 17156b and HD 80606b were both detected by Doppler surveys and both reside in highly eccentric orbits. HD 17156b has an orbital period of 21.2 days and an eccentricity of 0.67. This orbit carries the planet to a close stellar approach of 0.05 AU during periastron passage. HD 80606b is even more extreme; the orbital period of this planet is 111 days and the eccentricity is an extreme 0.9336. As a result, perias-



tron passage for this planet is only 0.03 AU from the host star. The orbits for HD 17156b (Fischer et al. 2007) and HD 80606b (Naef et al. 2001) were first determined from Doppler observations. This enabled a precise estimate of the transit times for what would have otherwise been a long-shot photometric campaign.

Transit observations measure the ratio of the planet radius to the stellar radius. In order to determine the mass and density of the exoplanet, this technique must be paired with radial velocity measurements. The combination of photometric transit detections and Keplerian modeling of radial velocity data is an example where the sum of two techniques far outweighs the contribution of either individual technique. Finally, it appears that another application of the RV technique is becoming more and more important in the context of transiting planets: the Rossiter-McLaughlin effect (see Chapter 4), which gives access to the spin-orbit geometry of the star-planet system and thus has the potential to probe its dynamical history.

### 3.5. Extending the Primary Mass Spectrum: Planets around M Dwarfs and Red Giants

The RV technique can also be applied to stars quite different from solar-type stars, provided enough Doppler information is available in their spectrum and stellar noise does not hide planetary signals. This allowed in particular for planet searches around stars with masses significantly different from  $1 M_{\odot}$ . The scientific motivation for this is the study of the formation and properties of exoplanets as a function of stellar mass. Protoplanetary disk masses are expected to scale with the mass of their central star, although the exact dependence is not known. As a consequence, theoretical models based on the core-accretion paradigm predict that gas giants should be rare around M dwarfs, but abundant around intermediate-mass stars (Laughlin et al. 2004, Ida & Lin 2005, Kennedy & Kenyon 2008).

Soon after the first discoveries of planets around FGK stars, new surveys started targeting nearby M dwarfs. For visible spectrographs, early M stars (M0 to M4) in the close solar neighborhood are still bright enough to allow for precise radial velocity measurements at the  $\sim 1 \text{ m s}^{-1}$  level. About 300–400 M stars with masses  $\sim 0.25\text{--}0.5 M_{\odot}$  have thus been monitored by different groups using instruments like OHP-ELODIE (Delfosse et al. 1998), Keck-HIRES (Marcy et al. 1998), ESO-CES/UVES (Kuerster et al. 1999), HET-HRS (Endl et al. 2006) and ESO-HARPS (Bonfils et al. 2005). These stars are however more active on average than FGK stars because the magnetic dynamo weakens more slowly with age compared to solar-type stars. Great care must therefore be taken in analyzing RV signals. Spectroscopic indicators such as CaII H&K and H $\alpha$  emission, and broadband photometry are useful diagnostics to assess the activity level, measure the stellar rotation period and disentangle planet-related and activity-related RV signals (e.g. Bonfils et al. 2007).

The first M dwarf found to be orbited by a planet was

GJ 876 (Delfosse et al. 1998, Marcy et al. 1998). It later turned out that the GJ 876 system is actually much more complex, with two giant planets in a 2:1 mean motion resonance (Marcy et al. 2001) and a close-in super-Earth (Rivera et al. 2005). However, this peculiar planetary system is not representative of the planet population that has been found around M dwarfs. In fact, only 4 such stars are known to harbor gas giants, which confirms the rarity of these objects around low-mass stars. On the other hand, several Neptune-mass planets and super-Earths have been found over the past few years (see Sect. 3.7), among which a quadruple system around GJ 581 (Udry et al. 2007). This points towards a significant difference between planet populations around Sun-like stars and M dwarfs (Bonfils et al. 2006, Endl et al. 2006, Johnson et al. 2007a). Protoplanetary disk masses are likely to be responsible for these differences, although metallicity may also play a role if M dwarfs had on average a lower metallicity (which is unclear).

On the other side of the stellar mass spectrum, i.e. for intermediate-mass stars, the radial velocity technique encounters several difficulties. In main-sequence A–F stars with  $M \gtrsim 1.5 M_{\odot}$ , the lower number of spectral features and their rotational broadening make it difficult to reach a high RV precision as far as photon noise is concerned. But more importantly, stellar pulsations and activity become the dominant source of noise and may hide planetary signals. A few RV surveys have nevertheless been targeting such stars with some success (e.g. Galland et al. 2005, 2006), but the planet detection limits are usually well above the  $1\text{--}M_{\text{Jup}}$  threshold.

Another strategy is to observe intermediate-mass stars in a later stage of their evolution, the red giant phase. They have then sufficiently cooled and slowed down to exhibit a rich spectrum with narrow spectral features. However, stellar noise again becomes the limiting factor for RV measurements, since red giants show p-mode oscillations with much larger amplitudes and periods than solar-type stars, have larger granulation noise and may also exhibit significant levels of RV jitter due to rotational modulations of photospheric features. Great care must therefore be taken in analyzing periodic RV signals in these stars, especially for the more evolved and luminous ones. Photometric and spectroscopic diagnostics should be used to check the planetary origin of RV signals.

Several surveys have been targeting giant stars, but with various sample definitions: nearby bright G and K giants (e.g. Hatzes & Cochran 1993, Frink et al. 2002, Setiawan et al. 2003, Sato et al. 2003, Doellinger et al. 2007, Niedziel-ski et al. 2007), subgiants (e.g. Johnson et al. 2007b) and open cluster giants (Lovis & Mayor 2007). Stellar masses in these samples vary from  $\sim 1$  to  $4 M_{\odot}$ , thereby opening a new domain in the parameter space. More than 20 planets have been detected around red giants and numbers are growing fast, showing a probable overabundance of “super-Jupiters” and a higher frequency of giant planets compared to solar-type stars (Lovis & Mayor 2007, Johnson et al. 2007a, Hekker et al. 2008). Fig. 3.5 illustrates this by

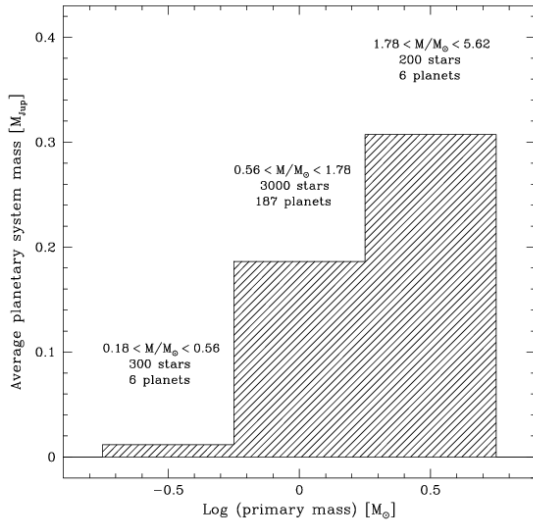


Fig. 7.— Average mass of planetary systems as a function of stellar mass, obtained by dividing, in each bin, the total (minimum) mass of all detected planets by the number of survey stars (from Lovis & Mayor 2007). The rising trend towards higher stellar masses shows that giant planets become more frequent and/or more massive with increasing stellar mass, in spite of detection biases towards higher-mass stars.

showing the average mass of planetary systems as a function of stellar mass. Although it does not give any details on the underlying planet population, the emerging trend clearly shows that stellar mass (and thus disk mass) plays an important role in the planet formation process. Other interesting properties of this population include a very different semi-major axis distribution, with no planets orbiting below  $\sim 0.7$  AU (Johnson et al. 2007b), and a possible lack of correlation between planet frequency and stellar metallicity (e.g. Pasquini et al. 2007). This latter point is however still debated.

### 3.6. The First Neptune-Mass Planets

In 2004, exoplanets made primarily of heavy elements instead of hydrogen were discovered for the first time, opening a new field of research and illustrating the capabilities of the radial velocity technique. Based on HARPS data, Santos et al. (2004) announced the detection of a hot Neptune orbiting the star  $\mu$  Ara in 9.6 days, a star already known to host two giant planets. Further measurements revealed yet another giant planet and established the minimum mass of the hot Neptune to be  $10.5 M_{\oplus}$  (Pepe et al. 2007). Simultaneously, McArthur et al. (2004) detected a close-in hot Neptune orbiting in 2.8 days around 55 Cnc, another star already known to harbor several giant planets. Fischer et al. (2008) then updated the orbital solutions for this sys-

tem, adding a fourth gas giant at intermediate distance and fixing the minimum mass of the hot Neptune to  $10.8 M_{\oplus}$ . 55 Cnc thus became the first known system with 5 planets. Both hot Neptune discoveries highlight the fact that such objects are well detectable with the RV technique, thanks to the improvements in precision and the gathering of a sufficient number of data points, a necessary condition to resolve the complex radial velocity curves of multi-planet systems. Both systems also hint to the fact that planets are rarely single, especially low-mass ones, and may very frequently appear in systems.

A third Neptune-mass object was discovered at the same time: GJ 436 b, orbiting an M dwarf on a close-in orbit with a period of 2.64 days and a minimum mass of  $23 M_{\oplus}$  (Butler et al. 2004). This minimum mass actually also became its true mass when Gillon et al. (2007) announced that the planet was transiting its host star. For the first time, the mass and radius of a Neptune-like planet could be measured, revealing an internal structure close to the one of Uranus and Neptune (mostly water ice with a H/He outer layer of  $\sim 10\%$  in mass). More details on this fascinating object are given in Sect. 3.4 and in the chapter on transiting planets.

### 3.7. Emergence of a New Population: Super-Earths and Ice Giants

The number of detected low-mass planets, Neptune-like or super-Earths, has been growing fast since 2004. Table 3.7 lists all objects with minimum masses below  $25 M_{\oplus}$  known as of June 2009. As can be seen, this is a rapidly evolving field of research, in which the HARPS spectrograph has made an essential contribution. These discoveries were made possible thanks to the sub- $\text{m s}^{-1}$  precision reached by this instrument. Indeed, most of these objects have RV semi-amplitudes  $K$  below  $3\text{--}4 \text{ m s}^{-1}$ , and have therefore been very difficult to detect with the previously-existing facilities that were limited to  $\sim 3 \text{ m s}^{-1}$ .

Among these low-mass objects, we note in particular the discovery of three systems containing at least three Neptunes or super-Earths, and no gas giants: HD 69830, GJ 581 and HD 40307. The triple-Neptune system HD 69830 was the first to be unveiled (Lovis et al. 2006). The first two planets orbit at 0.08 and 0.18 AU, while the third one is located further away at 0.62 AU. This shows that Neptune-mass objects are now detectable not only on close-in orbits, but all the way out to the habitable zone around solar-type stars. This however requires very high-precision RV measurements: the total RV dispersion before fitting any planet amounts to only  $3.7 \text{ m s}^{-1}$ . The post-fit residuals have a rms dispersion of  $0.8 \text{ m s}^{-1}$ , illustrating the unprecedented quality of the HARPS measurements. Fig. 3.7 shows a close-up view of the RV curve for this system, which reveals the complex nature and low amplitude of the RV variations. Besides precision, the acquisition of a large number of data points is also critical to resolve the three RV signals. The HD 69830 system appears as a new illustration of the diversity of planetary systems, with several Neptunes

Name	$K$ [m s <sup>-1</sup> ]	$m_2 \sin i$ [ $M_\oplus$ ]	$P$ [days]	$m_1$ [ $M_\odot$ ]	Instrument	Reference
GJ 581 e	1.9	1.9	3.15	0.31	HARPS	Mayor et al. (2009b)
HD 40307 b	2.0	4.2	4.31	0.77	HARPS	Mayor et al. (2009a)
GJ 581 c	3.2	5.4	12.9	0.31	HARPS	Udry et al. (2007)
GJ 876 d	2.7	5.7	1.94	0.32	HIRES	Rivera et al. (2005)
HD 40307 c	2.4	6.9	9.62	0.77	HARPS	Mayor et al. (2009a)
GJ 581 d	2.6	7.1	66.8	0.31	HARPS	Udry et al. (2007)
HD 181433 b	2.9	7.6	9.37	0.78	HARPS	Bouchy et al. (2009)
GJ 176 b	4.3	7.8	8.78	0.50	HARPS	Forveille et al. (2009)
HD 40307 d	2.6	9.2	20.5	0.77	HARPS	Mayor et al. (2009a)
HD 7924 b	3.9	9.3	5.40	0.83	HIRES	Howard et al. (2009)
HD 69830 b	3.6	10.5	8.67	0.86	HARPS	Lovis et al. (2006)
HD 160691 d	3.1	10.5	9.55	1.08	HARPS	Santos et al. (2004), Pepe et al. (2007)
55 Cnc e	3.7	10.8	2.82	1.03	HRS/HIRES	McArthur et al. (2004), Fischer et al. (2008)
GJ 674 b	8.7	11.8	4.69	0.35	HARPS	Bonfils et al. (2007)
HD 69830 c	2.9	12.1	31.6	0.86	HARPS	Lovis et al. (2006)
HD 4308 b	4.0	15.0	15.6	0.83	HARPS	Udry et al. (2006)
GJ 581 b	12.5	15.7	5.37	0.31	HARPS	Bonfils et al. (2005)
HD 190360 c	4.6	18.1	17.1	1.04	HIRES	Vogt et al. (2005)
HD 69830 d	2.2	18.4	197	0.86	HARPS	Lovis et al. (2006)
HD 219828 b	7.0	21.0	3.83	1.24	HARPS	Melo et al. (2007)
HD 16417 b	5.0	22.1	17.2	1.20	UCLES	O'Toole et al. (2009)
HD 47186 b	9.1	22.8	4.08	0.99	HARPS	Bouchy et al. (2009)
GJ 436 b	18.0	22.9	2.64	0.45	HIRES	Butler et al. (2004)
HAT-P-11 b	11.6	25.8	4.89	0.81	HAT/HIRES	Bakos et al. (2009)

Table 2: RV-detected exoplanets with minimum masses below  $25 M_\oplus$  as of June 2009, ordered according to their minimum mass.

on close-in orbits and no gas giants, at least within  $\sim 10$  AU. Its discovery immediately raised questions about the composition of the Neptunes, whether essentially rocky or icy, depending on where they were formed in the protoplanetary disk (Alibert et al. 2006). The interest in this system is further enhanced by the presence of a warm dust belt at  $\sim 1$  AU from the star, allowing for in-depth studies of the interactions between planets and debris disks (Beichman et al. 2005, Lisse et al. 2007).

GJ 581 is also a remarkable system, with a close-in Earth-mass planet, a hot Neptune and two super-Earths further away (Bonfils et al. 2005, Udry et al. 2007, Mayor et al. 2009b). With a minimum mass of only  $1.94 M_\oplus$ , GJ 581 e is presently the lowest-mass object ever discovered around a main-sequence star other than the Sun. The primary is an M dwarf with a mass of only  $0.31 M_\odot$ . As a consequence, it is easier to detect a planet of a given mass around this star compared to solar-type stars. Moreover, the habitable zone is expected to be much closer due to the lower stellar luminosity. The two super-Earths discovered at 0.07 and 0.22 AU are indeed located close to the inner and outer edges of this zone, which makes them arguably the two most "Earth-like" bodies known outside our Solar System. Obviously, too little is presently known about these objects, their atmospheres and their environment to decide if they resemble more the Earth, Venus, Mars or, more probably, something that is unknown in our Solar System (see e.g. Selsis et al. 2007 for a detailed discussion).

Mayor et al. (2009a) discovered yet another triple system, this time containing only super-Earths: HD 40307. With minimum masses of 4.2, 6.9 and  $9.2 M_\oplus$ , this is

the lowest-mass system known. Fig. 3.7 shows the phased radial velocity curves of these objects. The signal is extremely clear despite the very low amplitudes. This again shows that the RV technique has not reached its limits yet on such old and quiet solar-type stars. HD 40307 b has one of the lowest minimum masses and RV semi-amplitudes ( $2.0 \text{ m s}^{-1}$ ) among the known exoplanets. Even if its true mass is not known, this object is expected to be made exclusively of heavy elements (rocks and/or ices), being most probably not massive enough to retain a H/He atmosphere (especially under the intense irradiation from its host star).

Once more, nature has surprised us with the discoveries of these close-in, low-mass systems: their mere existence was not anticipated and is triggering further theoretical modeling to understand how and where they were formed, and what is their composition. Ice giants do exist in our Solar System, but at large orbital distances, while super-Earths occupy a completely unexplored mass range, where several mixtures of iron, silicates, ices and maybe hydrogen are possible.

From the observational point of view, it appears that a new population of low-mass planets is now emerging. Fig. 3.7 shows the mass distribution of all known exoplanets. It is obviously affected by several observational biases, but we are only interested here in its overall shape. Clearly, there seems to be an increase in population below  $20\text{--}30 M_\oplus$ , despite the strong bias of the RV technique towards low masses. Such an increase is also predicted by some theoretical simulations of planet formation based on the core-accretion model (e.g. Mordasini et al. 2009), while other models predict a large population only at lower masses (e.g.

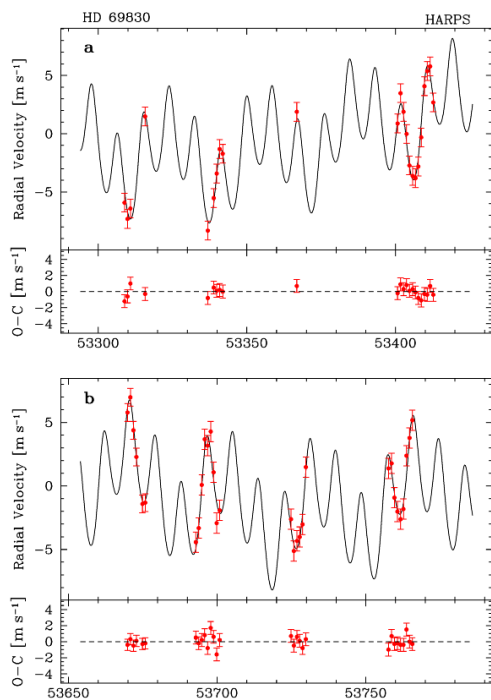


Fig. 8.— Close-up views of the HARPS radial velocity curve of HD 69830 as a function of time. The sub- $\text{m s}^{-1}$  precision of the data is critical to reveal the three low-amplitude RV signals caused by the orbiting Neptune-mass planets (from Lovis et al. 2006).

Ida & Lin 2008). In any case, the ongoing HARPS search for low-mass planets has detected many more candidates for which more measurements must be gathered to secure the orbital solutions (Lovis et al. 2009). Several tens of Neptunes and super-Earths are expected from this survey, the majority of which on close-in orbits within  $\sim 0.5$  AU. Most of them are also in multi-planet systems. Preliminary numbers indicate that the frequency of close-in low-mass planets around solar-type stars may be as high as  $\sim 30\%$  (Mayor et al. 2009a). Undoubtedly, the characterization of the low-mass population with the RV technique will bring many new constraints on our understanding of planet formation mechanisms. Moreover, it will allow us to put the Earth into the broader context of telluric planets in the Galaxy. Some outstanding issues that can be addressed with the present and near-future discoveries are:

- What is the precise mass distribution of the low-mass population at short distances? Are super-Earths more frequent than Neptunes?
- Are close-in Neptune-mass planets and super-Earths “failed” giant planet cores that could not accrete a massive H/He envelope?

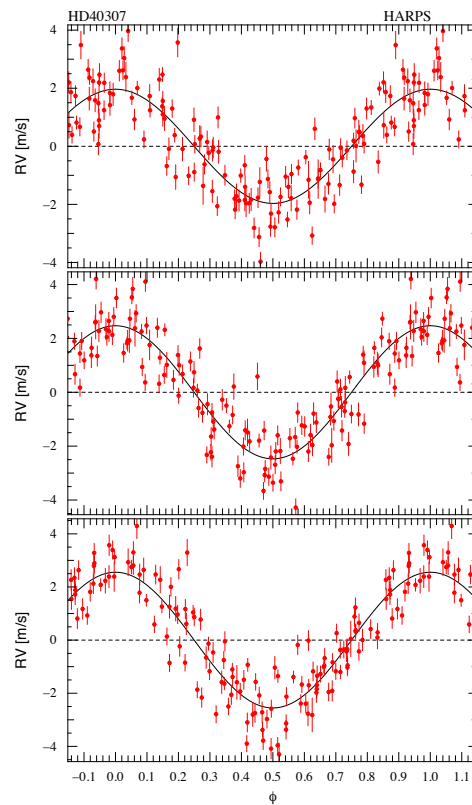


Fig. 9.— Phase-folded HARPS radial velocity curves of the three super-Earths orbiting HD 40307 (from Mayor et al. 2009a). In each case, the two other planets have been subtracted. Periods are 4.31, 9.62 and 20.5 days, while minimum masses are 4.2, 6.9 and 9.2  $M_{\oplus}$ , respectively.

- Have these objects formed beyond the ice line and subsequently migrated to their present location? Or can some of them have formed *in situ*, like telluric planets in our Solar System?
- Is there a correlation between orbital distance and planet mass? How do migration processes depend on planet mass?
- What are the relative frequencies of gas giants and low-mass planets? Is there a “desert” at intermediate masses?
- What is the eccentricity distribution of low-mass objects, and how does it compare to gas giants?
- Are stars hosting low-mass planets preferentially metal-rich? Is there any correlation between stellar parameters and the presence of low-mass planets?
- What is the dynamical architecture of multi-planet systems, and what is their dynamical history?

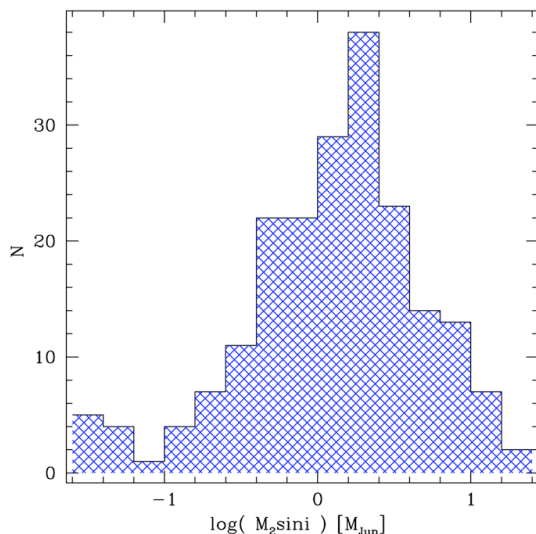


Fig. 10.— Observed mass distribution of all known exoplanets. A hint of an increase in population below 20–30  $M_{\oplus}$  is clearly visible, despite strong observational biases at low masses.

- Are low-mass planets more or less common around M dwarfs compared to solar-type stars? What is their frequency in the habitable zone of M dwarfs?

The list can be continued indefinitely. The rapidly growing number of known low-mass planets should soon allow us to unveil the main statistical properties of this population. Finally, it has to be noted that RV surveys are targeting nearby bright stars, and every discovered close-in Neptune or super-Earth should be considered as a potentially extremely interesting transiting candidate. Transits are rare due to the low geometric probabilities, but the few low-mass objects that do transit a nearby bright star will probably represent “Rosetta stones” for our understanding of exoplanets. They will likely be discovered by RV surveys and follow-up photometry. However, space-based photometry is necessary to reach the precision required to detect the very small transit depths caused by these objects. Given the wealth of information that can be obtained from transits and anti-transits on a bright star (precise density, composition and temperature, in-depth atmospheric studies), the scientific return is certainly worth the effort.

## 4. FUTURE PROSPECTS

### 4.1. Alternative RV Techniques

#### 4.1.1. Radial Velocities in the Near-IR

Radial velocity planet surveys of M dwarf stars have substantial scientific merit because these are the most common stars in our galaxy. In principle, there is a two-fold enhancement in the detectability of rocky planets at habitable

zone distances. Compared with solar mass stars, the reflex stellar velocity for lower mass M dwarf stars is greater by a factor of about three. The stellar velocity amplitude is further increased because of the proximity of the habitable zone to these low luminosity stars. However, at optical wavelengths, late-type M dwarfs are faint stars. The flux of M4V stars peaks in the 1–2  $\mu\text{m}$  wavelength range. An M4V star at a distance of 20 parsecs has a V-band magnitude of 14, but a J-band magnitude of 9. Therefore, these stars are challenging targets for optical spectroscopy even with 10-m telescopes, but accessible with IR spectroscopy on even moderate aperture telescopes.

There are still challenges for IR spectroscopy. Telluric absorption lines litter the IR spectrum and vary with the changing column density of water vapor on timescales of hours. Rotational velocity rises for stars later in spectral type than M4V, resulting in broader spectral lines. And flares are common sources of astrophysical noise for stars at the end of the main sequence. Nevertheless, technology development is ongoing to advance IR spectroscopy to precisions below  $10 \text{ m s}^{-1}$ , and the field is making rapid progress. Several authors have recently achieved  $\sim 5 \text{ m s}^{-1}$  precision using the CRIRES instrument at the VLT, a high-resolution near-IR slit spectrograph (Kaufl et al. 2004). On the one hand, Huelamo et al. (2008) and Figueira et al. (2010) use telluric  $\text{CO}_2$  lines in the  $H$  band as wavelength references, and select unblended stellar lines to compute radial velocities via the cross-correlation method. On the other hand, Bean et al. (2009) have developed a procedure that is similar to the iodine method in the visible. Using an ammonia gas cell in the  $K$  band, they model the observed spectrum as a combination of the stellar, ammonia and telluric spectrum, convolved with the instrument PSF. Both approaches had to deal with broadly similar challenges as in the visible: the varying spectrograph illumination and the need for a suitable wavelength reference. Besides these two aspects, the dense telluric spectrum clearly represents a supplementary difficulty in the near-IR.

These recent results are nevertheless very encouraging and there is little doubt that further progress will occur soon in this field, especially considering the development of several new high-resolution near-IR spectrographs. Radial velocities in the near-IR should become an optimal technique for the detection of planets around stars later than M4V in the near future.

#### 4.1.2. Dispersed fixed-delay interferometry

The dispersed fixed delay interferometer (DFDI) combines a moderate-dispersion spectrograph with a Michelson type interferometer, adding a graded phase delay perpendicular to the dispersion direction which creates fringes in each resolution element. Doppler shifts cause the fringes in each resolution element to move, allowing a measurement of the radial velocity (Erskine & Ge 2000; Ge 2002; Ge et al. 2002). This Doppler measurement approach is completely different from the echelle approach which measures

the absorption line centroid shifts. The Doppler sensitivity of the DFDI approach weakly depends on the spectral resolution compared to the echelle approach (1/2 power of the spectral resolution vs. 3/2 power of the spectral resolution in the echelle method, Ge 2002). This allows the use of a medium resolution, but high efficiency spectrometer for dispersing the fringes to boost the overall detection efficiency, while reducing the instrument size and cost. Also, the DFDI approach takes up a small amount of space on a CCD to cover one dispersion order fringing spectrum with a moderate wavelength coverage (e.g.  $\sim 600 \text{ \AA}$  for the Exoplanet Tracker instrument at the Kitt Peak National Observatory 2.1 meter telescope, Ge et al. 2006), which allows to either use a multi-object fiber feed so that simultaneous, high-throughput, high Doppler sensitivity measurements of many objects may be made with reasonable detector sizes or implement a cross-dispersion mode for large wavelength coverage, high dispersion, high throughput and high Doppler sensitivity measurements of a single star (Ge 2002; Ge et al. 2007).

To date, one planet has been discovered by the DFDI instruments, around the star HD 102195 (Ge et al. 2006). Several planet and brown dwarf candidates have been identified from the on-going planet surveys at the Sloan Digital Sky Survey telescope and the KPNO 2.1m telescope and are being followed up with additional observations. A next-generation, multiple-object, DFDI Doppler instrument with 60 object capability was commissioned at the SDSS telescope at Apache Point Observatory in September 2008 and is being used for conducting the Multi-object APO Radial-Velocity Exoplanet Large-area Survey (MARVELS), which is one of the four Sloan Digital Sky Survey (SDSS) III survey projects in the period 2008-2014.

#### 4.2. Characterization of Transiting Planets Found by Space Missions

The space missions CoRoT and Kepler (Baglin et al. 2002, Borucki et al. 2003) are both dedicated to the search of transiting exoplanets by collecting long, high-precision photometric time series of thousands of stars. Transit events have to pass first through a series of photometric and spectroscopic tests to exclude alternative scenarios before they can be confirmed as *bona fide* transiting planets. High-precision radial velocity measurements are then necessary to measure the mass of the objects and obtain their mean density. This follow-up work has already been ongoing with great success for CoRoT and several ground-based transit surveys, which are presently discovering a large number of hot Jupiters (e.g. SWASP, HAT). CoRoT and particularly Kepler are expected to also find several hot Neptunes and super-Earths, whose mass will have to be measured. This task may be challenging due to the faintness of the targets and their activity level. However, for quiet stars with magnitudes  $V=11-12$ , instruments like HARPS and its twin HARPS-North (Latham et al. 2007) will be able to measure the masses of close-in super-Earths down to

$\sim 5 M_{\oplus}$  with an accuracy ( $\sim 10\%$ ) that should be sufficient to usefully constrain their mean density and composition. In the near future, the combination of space-based transit searches and high-precision RV follow-up is thus likely to considerably improve our knowledge of the close-in low-mass planet population.

#### 4.3. Pushing down the Limits: towards the Detection of Earths around Nearby Stars

What are the ultimate limitations of the radial velocity technique? To answer this difficult question, it is necessary to identify which are the dominant sources of systematic errors. These fall into two general categories: instrumental and stellar. We first discuss the instrumental aspects, and then examine stellar noise.

Instrumental limitations are presently fairly well understood, and strategies to overcome them are being developed. For HARPS-like instruments, the limiting factors are mainly the guiding system, the light-scrambling efficiency and the wavelength calibration source. For each of these issues, it appears that significant progress is possible compared to existing facilities like HARPS with relatively modest technological developments and costs. Tests are ongoing on optimized light injection optics and optical fibers to make the spectrograph illumination as homogeneous as possible. As for wavelength calibration, new solutions such as the laser frequency comb (see Sect. 2.5) and stabilized Fabry-Pérot etalons are being developed and tested.

Two major European instrumental projects are now building on the HARPS experience with the goal of improving the overall stability and precision, but also the photon collecting power. Indeed, HARPS is not far from being photon-limited on the typical stars that are presently searched for low-mass planets, so that a larger telescope aperture is needed if performances are to be significantly improved. The first of these projects is ESPRESSO, the successor of HARPS, to be installed on the ESO Very Large Telescope at Paranal Observatory, Chile (Pepe et al. 2010). ESPRESSO is developed with the goal of achieving an instrumental precision of  $10 \text{ cm s}^{-1}$  on both the short- and long-term, corresponding to the RV signal induced by the Earth orbiting the Sun. Moreover, ESPRESSO will benefit from the large 8.2m aperture of the VLT. It will even be possible to feed the spectrograph with the four 8.2m telescopes simultaneously, which represent the equivalent of a single 16m aperture. In this mode, the radial velocity precision will however be somewhat degraded compared to the single-telescope mode. According to the typical numbers given in Sect. 2.3, it appears that a SNR of about 700 per pixel will be required (at 550 nm) to achieve a photon-limited precision of  $10 \text{ cm s}^{-1}$  at  $R = 140,000$ . This can be obtained in about 20 min of exposure time for stars with  $V=7.5$  on a 10-m class telescope. ESPRESSO will thus be able to carry out an extremely precise survey of 100-200 nearby bright stars, carefully selected to minimize stellar noise based on HARPS data. It will find all low-mass plan-

ets down to a few Earth masses orbiting within  $\sim 1$  AU of their parent star, and possibly even  $1-M_{\oplus}$  planets in the habitable zones around K and M dwarfs. This survey should thus yield a comprehensive picture of telluric planets in the solar neighborhood.

The other major European project is CODEX, an ultra-stable high-resolution visible spectrograph for the European Extremely Large Telescope (Pasquini et al. 2008). The aimed instrumental precision of CODEX is  $\sim 1 \text{ cm s}^{-1}$ . Its main science objectives all require extremely high Doppler precision: measurement of the cosmological redshift drift and the dynamics of the Universe, search for Earth-like planets and search for variability in fundamental constants. Although the required performances are quite challenging, there is little doubt that the possibility to address these outstanding scientific issues is well worth the technical effort. The experience gained with HARPS and ESPRESSO is expected to be of great value in this context.

We now turn to the issue of stellar noise in the context of the detection of very low-amplitude radial velocity signals. As described in Sect. 2.4, several physical phenomena in stellar photospheres (oscillations, granulation, active regions) may hide planet-induced RV variations at the  $\text{m s}^{-1}$  level and below. To address this problem, studies are ongoing to precisely characterize stellar RV noise at the relevant timescales (from minutes for oscillations to about one month for activity). Solar and stellar power density spectra of long, high-precision RV time series can be used to derive the main properties of each noise component and understand how it varies from star to star. From these results it is possible to find and select the most suitable stars for sub- $\text{m s}^{-1}$  RV monitoring. From what is presently known about stellar noise, it clearly appears that F stars and slightly evolved G and K stars are unsuitable because all noise sources become larger in these objects. Between unevolved-G and M stars, oscillation and granulation noise become smaller, but activity levels tend to be higher in late-K and M stars because of the slower decrease of activity with age. However, this is partly compensated by the lower masses of these stars which make RV signals larger for a given planet mass. Activity-related noise can be minimized by selecting the stars with the lowest CaII H&K index, and in particular those which do not exhibit activity cycles (or only weak ones). Such objects may be in a Maunder-minimum state, an optimal situation to reach unprecedented precision levels on RV measurements. The identification of this low-activity population is presently ongoing, making use of the thousands of spectra that have been gathered by radial velocity surveys over the past years.

Realistic simulations of the stellar noise, based on observed power density spectra, should be made to derive the optimal observing strategy and compute planet detection limits (e.g. Dumusque et al. 2010, in preparation). Preliminary results indicate that a sufficiently dense sampling properly covering the typical timescales of the different noise sources lead to significant improvements in planet detection limits. Moreover, the search for planets in the habit-

able zone may well benefit from the probably low stellar noise level over timescales of 100-1000 days. As a result, it may well be possible to detect Earth-mass planets in the habitable zone of G, and particularly K dwarfs. Despite the low RV amplitudes, solar-like stars should therefore also be considered for this kind of searches, together with M dwarfs which have the obvious advantages of being less massive and having closer habitable zones. Finally, we note that these estimates are not only the result of simulations, but also of real data: as an example, binning the HARPS RV measurements obtained on the star HD 69830 (Lovis et al. 2006) over timescales of  $\sim 15$  days yields a long-term RV dispersion of only  $\sim 30 \text{ cm s}^{-1}$  (after subtracting the signal of the three known planets). Given all the instrumental error sources and photon noise that contribute to this number, this observational result shows that we are indeed tantalizingly close to being able to detect an Earth-like planet in the habitable zone of this star.

#### 4.4. Conclusion

In this chapter we have reviewed the history, capabilities, achievements and present state-of-the-art of the radial velocity technique applied to the search for exoplanets. In summary this technique has, over the past 15 years, opened and developed a new field of astrophysics which has already become one of the most prominent in this discipline, be it in terms of its scientific potential or in terms of the wide-ranging public interest associated to it. After the initial gas giant era, the RV technique has now fully entered the domain of low-mass planets. Given the achieved detection limits, present and near-future RV surveys of nearby bright stars will unveil the statistical properties of the low-mass planet population within  $\sim 1$  AU. We will then have a global picture of exoplanets, from massive gas giants to telluric bodies, and this will allow us to make decisive steps in our understanding of planet formation and migration. This is all the more true in cases where the RV technique can be coupled to the transit technique. As other detection techniques appear and are developed, radial velocities will remain a fundamental tool to obtain dynamical masses and characterize systems. As an important by-product, the obtained high-resolution spectra can be used to characterize the host star. Detecting exoplanets is and will remain an observational challenge requiring significant efforts in instrumental developments. While all possible approaches should certainly be explored, the cost-effectiveness of the RV technique should be particularly emphasized, and thus the development of improved RV facilities should certainly be continued in the future.

#### Acknowledgments.



## REFERENCES

- Alibert, Y., Baraffe, I., Benz, W., et al. (2006) Formation and structure of the three Neptune-mass planets system around HD 69830. *Astron. Astrophys.*, **455**, L25-L28.
- Baglin, A., Auvergne, M., Barge, P., et al. (2002) COROT: asteroseismology and planet finding. In *Proceedings of the First Eddington Workshop on Stellar Structure and Habitable Planet Finding*, *ESA Spec. Publ.*, **485** (B. Battrick et al., eds.), 17-24.
- Bakos, G. Á., Torres, G., Pál, A., et al. (2010) HAT-P-11b: A Super-Neptune Planet Transiting a Bright K Star in the Kepler Field. Accepted for publication in *Astrophys. J.*, arXiv:0901.0282.
- Baliunas, S. L., Donahue, R. A., Soon, W. H., et al. (1995) Chromospheric variations in main-sequence stars. *Astrophys. J.*, **438**, 269-287.
- Baranne, A., Queloz, D., Mayor, M., et al. (1996) ELODIE: A spectrograph for accurate radial velocity measurements.. *Astron. Astrophys. Supp. Ser.*, **119**, 373-390.
- Bean, J. L., Seifahrt, A., Hartman, H., et al. (2009) The CRIRES Search for Planets Around the Lowest-Mass Stars. I. High-Precision Near-Infrared Radial Velocities with an Ammonia Gas Cell. *Astrophys. J.*, in press, arXiv:0911.3148.
- Beichman, C. A., Bryden, G., Gautier, T. N., et al. (2005) An Excess Due to Small Grains around the Nearby K0 V Star HD 69830: Asteroid or Cometary Debris? *Astrophys. J.*, **626**, 1061-1069.
- Blake, C. (2008) UNKNOWN REFERENCE
- Bonfils, X., Delfosse, X., Udry, S., et al. (2006) Any hot-Jupiter around M dwarfs? In *Tenth Anniversary of 51 Peg-b: Status of and prospects for hot Jupiter studies* (L. Arnold et al., eds.), 111-118.
- Bonfils, X., Forveille, T., Delfosse, X., et al. (2005) The HARPS search for southern extra-solar planets. VI. A Neptune-mass planet around the nearby M dwarf Gl 581. *Astron. Astrophys.*, **443**, L15-L18.
- Bonfils, X., Mayor, M., Delfosse, X., et al. (2007) The HARPS search for southern extra-solar planets. X. A  $m \sin i = 11 M_{\oplus}$  planet around the nearby spotted M dwarf GJ 674. *Astron. Astrophys.*, **474**, 293-299.
- Borucki, W. J., Koch, D. G., Lissauer, J. J., et al. (2003) The Kepler mission: a wide-field-of-view photometer designed to determine the frequency of Earth-size planets around solar-like stars. In *Future EUV/UV and Visible Space Astrophysics Missions and Instrumentation*, *Proc. Soc. Photo-Opt. Instrum. Eng.*, **4854** (J.C. Blades et al., eds.), 129-140.
- Bouchy, F., and Carrier, F. (2001) P-mode observations on  $\alpha$  Cen A. *Astron. Astrophys.*, **374**, L5-L8.
- Bouchy, F., Pepe, F., and Queloz, D. (2001) Fundamental photon noise limit to radial velocity measurements. *Astron. Astrophys.*, **374**, 733-739.
- Bouchy, F., Mayor, M., Lovis, C., et al. (2009) The HARPS search for southern extra-solar planets. XVII. Super-Earth and Neptune-mass planets in multiple planet systems HD 47 186 and HD 181 433. *Astron. Astrophys.*, **496**, 527-531.
- Bouchy, F., and The Sophie Team (2006) SOPHIE: the successor of the spectrograph ELODIE for extrasolar planet search and characterization. In *Tenth Anniversary of 51 Peg-b: Status of and prospects for hot Jupiter studies* (L. Arnold et al., eds.), 319-325.
- Braje, D. A., Kirchner, M. S., Osterman, S., et al. (2008) Astronomical spectrograph calibration with broad-spectrum frequency combs. *Eur. Phys. J. D*, **48**, 57-66.
- Butler, R. P., and Marcy, G. W. (1996) A Planet Orbiting 47 Ursae Majoris. *Astrophys. J. Lett.*, **464**, L153-L156.
- Butler, R. P., Marcy, G. W., Williams, E., et al. (1996) Attaining Doppler Precision of  $3 \text{ m s}^{-1}$ . *Publ. Astron. Soc. Pac.*, **108**, 500-509.
- Butler, R. P., Marcy, G. W., Williams, E., et al. (1997) Three New "51 Pegasi-Type" Planets. *Astrophys. J. Lett.*, **474**, L115-L118.
- Butler, R. P., Vogt, S. S., Marcy, G. W., et al. (2004) A Neptune-Mass Planet Orbiting the Nearby M Dwarf GJ 436. *Astrophys. J.*, **617**, 580-588.
- Campbell, B. and Walker, G. A. H (1979) Precision radial velocities with an absorption cell. *Publ. Astron. Soc. Pac.*, **91**, 540-545.
- Campbell, B., Walker, G. A. H., and Yang, S. (1988) A search for substellar companions to solar-type stars. *Astrophys. J.*, **331**, 902-921.
- Charbonneau, D., Brown, T. M., Latham, D. W., et al. (2000) Detection of Planetary Transits Across a Sun-like Star. *Astrophys. J. Lett.*, **529**, L45-L48.
- Christensen-Dalsgaard, J. (2004) Physics of solar-like oscillations. In *Sol. Phys.*, **220**, Issue 2, 137-168.
- Connes, P. (1985) Absolute astronomical accelerometry. *Astrophys. Space Sci.*, **110**, 211-255.
- Delfosse, X., Forveille, T., Mayor, M., et al. (1998) The closest extrasolar planet. A giant planet around the M4 dwarf GL 876. *Astron. Astrophys.*, **338**, L67-L70.
- Desort, M., Lagrange, A.-M., Galland, F., et al. (2007) Search for exoplanets with the radial-velocity technique: quantitative diagnostics of stellar activity. *Astron. Astrophys.*, **473**, 983-993.
- Döllinger, M. P., Hatzes, A. P., Pasquini, L., et al. (2007) Discovery of a planet around the K giant star 4 Ursae Majoris. *Astron. Astrophys.*, **472**, 649-652.
- Dravins, D. (1990) Stellar granulation. VI - Four-component models and non-solar-type stars. *Astron. Astrophys.*, **228**, 218-230.
- Einstein, A. (1905) Zur Elektrodynamik bewegter Körper. *Ann. Phys.*, **322**, 891-921.
- Endl, M., Cochran, W. D., Kürster, M., et al. (2006) Exploring the Frequency of Close-in Jovian Planets around M Dwarfs. *Astrophys. J.*, **649**, 436-443.
- Erskine, D. J., and Ge, J. (2000) A Novel Interferometer Spectrometer for Sensitive Stellar Radial Velocimetry. In *Imaging the Universe in Three Dimensions*, *Publ. Astron. Soc. Pac. Conf. Ser.*, **195** (W. van Breugel and J. Bland-Hawthorn, eds.), 501-507.
- Fienga, A., Manche, H., Laskar, J., et al. (2008) INPOP06: a new numerical planetary ephemeris. *Astron. Astrophys.*, **477**, 315-327.
- Figueira, P., Pepe, F., Melo, C. H. F., et al. (2009) Radial Velocities with CRIRES: Pushing precision down to 5-10 m/s. *Astron. Astrophys.*, in press, arXiv:0912.2643.
- Fischer, D. A., Marcy, G. W., Butler, R. P., et al. (2008) Five Planets Orbiting 55 Cancri. *Astrophys. J.*, **675**, 790-801.
- Fischer, D. A., Vogt, S. S., Marcy, G. W., et al. (2007) Five Intermediate-Period Planets from the N2K Sample. *Astrophys. J.*, **669**, 1336-1344.
- Forveille, T., Bonfils, X., Delfosse, X., et al. (2009) The HARPS search for southern extra-solar planets. XIV. Gl 176b, a super-Earth rather than a Neptune, and at a different period. *Astron.*



- Astrophys.*, 493, 645-650.
- Frink, S., Mitchell, D. S., Quirrenbach, A., et al. (2002) Discovery of a Substellar Companion to the K2 III Giant  $\iota$  Draconis. *Astrophys. J.*, 576, 478-484.
- Galland, F., Lagrange, A.-M., Udry, S., et al. (2005) Extrasolar planets and brown dwarfs around A-F type stars. II. A planet found with ELODIE around the F6V star HD 33564. *Astron. Astrophys.*, 444, L21-L24.
- Galland, F., Lagrange, A.-M., Udry, S., et al. (2006) Extrasolar planets and brown dwarfs around A-F type stars. IV. A candidate brown dwarf around the A9V pulsating star HD 180777. *Astron. Astrophys.*, 452, 709-714.
- Ge, J. (2002) Fixed Delay Interferometry for Doppler Extrasolar Planet Detection. *Astrophys. J. Lett.*, 571, L165-L168.
- Ge, J., Erskine, D. J., and Rushford, M. (2002) An Externally Dispersed Interferometer for Sensitive Doppler Extrasolar Planet Searches. *Publ. Astron. Soc. Pac.*, 114, 1016-1028.
- Ge, J., van Eyken, J., Mahadevan, S., et al. (2006) The First Extrasolar Planet Discovered with a New-Generation High-Throughput Doppler Instrument. *Astrophys. J.*, 648, 683-695.
- Ge, J., van Eyken, J. C., Mahadevan, S., et al. (2007) An All Sky Extrasolar Planet Survey with New Generation Multiple Object Doppler Instruments at Sloan Telescope. *Rev. Mex. Astron. Astrophys. Conf. Ser.*, 29, 30-36.
- Gillon, M., Pont, F., Demory, B.-O., et al. (2007) Detection of transits of the nearby hot Neptune GJ 436 b. *Astron. Astrophys.*, 472, L13-L16.
- Griffin, R. and Griffin, R. (1973) Accurate wavelengths of stellar and telluric absorption lines near  $\lambda$  7000 Angstroms. *Mon. Not. Roy. Astr. Soc.*, 162, 255-260.
- Hatzes, A. P., and Cochran, W. D. (1993) Long-period radial velocity variations in three K giants. *Astrophys. J.*, 413, 339-348.
- Hekker, S., Snellen, I. A. G., Aerts, C., et al. (2008) Precise radial velocities of giant stars. IV. A correlation between surface gravity and radial velocity variation and a statistical investigation of companion properties. *Astron. Astrophys.*, 480, 215-222.
- Henry, G. W., Marcy, G. W., Butler, R. P., et al. (2000) A Transiting "51 Peg-like" Planet. *Astrophys. J. Lett.*, 529, L41-L44.
- Howard, A. W., Johnson, J. A., Marcy, G. W., et al. (2009) The NASA-UC Eta-Earth Program. I. A Super-Earth Orbiting HD 7924. *Astrophys. J.*, 696, 75-83.
- Huélamo, N., Figueira, P., Bonfils, X., et al. (2008) TW Hydrae: evidence of stellar spots instead of a Hot Jupiter. *Astron. Astrophys.*, 489, L9-L13.
- Ida, S., and Lin, D. N. C. (2005) Toward a Deterministic Model of Planetary Formation. III. Mass Distribution of Short-Period Planets around Stars of Various Masses. *Astrophys. J.*, 626, 1045-1060.
- Ida, S., and Lin, D. N. C. (2008) Toward a Deterministic Model of Planetary Formation. V. Accumulation Near the Ice Line and Super-Earths. *Astrophys. J.*, 685, 584-595.
- Johnson, J. A., Butler, R. P., Marcy, G. W., et al. (2007a) A New Planet around an M Dwarf: Revealing a Correlation between Exoplanets and Stellar Mass. *Astrophys. J.*, 670, 833-840.
- Johnson, J. A., Fischer, D. A., Marcy, G. W., et al. (2007b) Retired A Stars and Their Companions: Exoplanets Orbiting Three Intermediate-Mass Subgiants. *Astrophys. J.*, 665, 785-793.
- Kaeufl, H.-U., Ballester, P., Biereichel, P., et al. (2004) CRIRES: a high-resolution infrared spectrograph for ESO's VLT. In *Ground-based Instrumentation for Astronomy, Proc. Soc. Photo-Opt. Instrum. Eng.*, 5492 (A.F.M. Moorwood and I. Masanori, eds.), 1218-1227.
- Kennedy, G. M., and Kenyon, S. J. (2008) Planet Formation around Stars of Various Masses: The Snow Line and the Frequency of Giant Planets. *Astrophys. J.*, 673, 502-512.
- Kjeldsen, H., Bedding, T. R., Butler, R. P., et al. (2005) Solar-like Oscillations in  $\alpha$  Centauri B. *Astrophys. J.*, 635, 1281-1290.
- Kürster, M., Hatzes, A. P., Cochran, W. D., et al. (1999) Precise radial velocities of Proxima Centauri. Strong constraints on a substellar companion. *Astron. Astrophys.*, 344, L5-L8.
- Latham, D. W. (2007) Hot Earths: Prospects For Detection By Kepler And Characterization with HARPS-NEF. *Bull. Am. Astron. Soc.*, 38, 234.
- Latham, D. W., Stefanik, R. P., Mazeh, T., et al. (1989) The unseen companion of HD114762 - A probable brown dwarf. *Nature*, 339, 38-40.
- Laughlin, G., Bodenheimer, P., and Adams, F. C. (2004) The Core Accretion Model Predicts Few Jovian-Mass Planets Orbiting Red Dwarfs. *Astrophys. J. Lett.*, 612, L73-L76.
- Li, C.-H., Benedict, A. J., Fendel, P., et al. (2008) A laser frequency comb that enables radial velocity measurements with a precision of  $1 \text{ cm s}^{-1}$ . *Nature*, 452, 610-612.
- Lindgren, L., and Dravins, D. (2003) The fundamental definition of "radial velocity". *Astron. Astrophys.*, 401, 1185-1201.
- Lisse, C. M., Beichman, C. A., Bryden, G., et al. (2007) On the Nature of the Dust in the Debris Disk around HD 69830. *Astrophys. J.*, 658, 584-592.
- Lovis, C., and Pepe, F. (2007) A new list of thorium and argon spectral lines in the visible. *Astron. Astrophys.*, 468, 1115-1121.
- Lovis, C., and Mayor, M. (2007) Planets around evolved intermediate-mass stars. I. Two substellar companions in the open clusters NGC 2423 and NGC 4349. *Astron. Astrophys.*, 472, 657-664.
- Lovis, C., Mayor, M., Bouchy, F., et al. (2009) Towards the characterization of the hot Neptune/super-Earth population around nearby bright stars. In *Transiting Planets, Proc. Int. Astron. Union*, 253, 502-505.
- Lovis, C., Mayor, M., Pepe, F., et al. (2006) An extrasolar planetary system with three Neptune-mass planets. *Nature*, 441, 305-309.
- Marcy, G. W., and Butler, R. P. (1995) The Planet around 51 Pegasi. *Bull. Am. Astron. Soc.*, 27, 1379.
- Marcy, G. W., and Butler, R. P. (1996) A Planetary Companion to 70 Virginis. *Astrophys. J. Lett.*, 464, L147-L151.
- Marcy, G. W., Butler, R. P., Fischer, D., et al. (2001) A Pair of Resonant Planets Orbiting GJ 876. *Astrophys. J.*, 556, 296-301.
- Marcy, G. W., Butler, R. P., Vogt, S. S., et al. (1998) A Planetary Companion to a Nearby M4 Dwarf, Gliese 876. *Astrophys. J. Lett.*, 505, L147-L149.
- Mayor, M., Bonfils, X., Forveille, T., et al. (2009b) The HARPS search for southern extra-solar planets. XVIII. An Earth-mass planet in the GJ 581 planetary system. *Astron. Astrophys.*, 507, 487-494.
- Mayor, M., Pepe, F., Queloz, D., et al. (2003) Setting New Standards with HARPS. *The Messenger*, 114, 20-24.
- Mayor, M., and Queloz, D. (1995) A Jupiter-mass companion to a solar-type star. *Nature*, 378, 355-359.
- Mayor, M., Udry, S., Lovis, C., et al. (2009a) The HARPS search for southern extra-solar planets. XIII. A planetary system with 3 super-Earths (4.2, 6.9, and 9.2  $M_{\oplus}$ ). *Astron. Astrophys.*, 493, 639-644.
- McArthur, B. E., Endl, M., Cochran, W. D., et al. (2004) Detection

- of a Neptune-Mass Planet in the  $\rho^1$  Cancri System Using the Hobby-Eberly Telescope. *Astrophys. J. Lett.*, 614, L81-L84.
- Melo, C., Santos, N. C., Gieren, W., et al. (2007) A new Neptune-mass planet orbiting HD 219828. *Astron. Astrophys.*, 467, 721-727.
- Mordasini, C., Alibert, Y., Benz, W., et al. (2009) Extrasolar planet population synthesis. I. Method, formation tracks, and mass-distance distribution. *Astron. Astrophys.*, 501, 1139-1160.
- Murphy, M. T., Udem, T., Holzwarth, R., et al. (2007) High-precision wavelength calibration of astronomical spectrographs with laser frequency combs. *Mon. Not. Roy. Astr. Soc.*, 380, 839-847.
- Naef, D., Latham, D. W., Mayor, M., et al. (2001) HD 80606 b, a planet on an extremely elongated orbit. *Astron. Astrophys.*, 375, L27-L30.
- Niedzielski, A., Konacki, M., Wolszczan, A., et al. (2007) A Planetary-Mass Companion to the K0 Giant HD 17092. *Astrophys. J.*, 669, 1354-1358.
- O'Toole, S., Tinney, C. G., Butler, R. P., et al. (2009) A Neptune-mass Planet Orbiting the Nearby G Dwarf HD 16417. *Astrophys. J.*, 697, 1263-1268.
- Pallé, P. L., Jimenez, A., Perez Hernandez, F., et al. (1995) A measurement of the background solar velocity spectrum. *Astrophys. J.*, 441, 952-959.
- Pasquini, L., Avila, G., Dekker, H., et al. (2008) CODEX: the high-resolution visual spectrograph for the E-ELT. In *Ground-based and Airborne Instrumentation for Astronomy II*, Proc. Soc. Photo-Opt. Instrum. Eng., 7014 (I.S. McLean and M.M. Casali, eds.), 70141I.
- Pasquini, L., Döllinger, M. P., Weiss, A., et al. (2007) Evolved stars suggest an external origin of the enhanced metallicity in planet-hosting stars. *Astron. Astrophys.*, 473, 979-982.
- Pepe, F., Correia, A. C. M., Mayor, M., et al. (2007) The HARPS search for southern extra-solar planets. VIII.  $\mu$  Arae, a system with four planets. *Astron. Astrophys.*, 462, 769-776.
- Pepe, F., Mayor, M., Galland, F., et al. (2002) The CORALIE survey for southern extra-solar planets VII. Two short-period Saturnian companions to HD 108147 and HD 168746. *Astron. Astrophys.*, 388, 632-638.
- Pepe, F., Cristiani, S., Rebolo Lopez, R., et al. (2010) ESPRESSO - Exploring science frontiers with extreme-precision spectroscopy. In *Ground-based and Airborne Instrumentation for Astronomy III*, Proc. Soc. Photo-Opt. Instrum. Eng., in press (I.S. McLean et al., eds.).
- Queloz, D., Henry, G. W., Sivan, J. P., et al. (2001) No planet for HD 166435. *Astron. Astrophys.*, 379, 279-287.
- Queloz, D., Mayor, M., Weber, L., et al. (2000) The CORALIE survey for southern extra-solar planets. I. A planet orbiting the star Gliese 86. *Astron. Astrophys.*, 354, 99-102.
- Rickman, H. (2001) Transactions of the International Astronomical Union Proceedings of the Twenty-Fourth General Assembly. In *Transactions of the International Astronomical Union*, Astron. Soc. Pac. Ser. B, 24 (H. Rickman, ed.).
- Rivera, E. J., Lissauer, J. J., Butler, R. P., et al. (2005) A 7.5  $M_{\oplus}$  Planet Orbiting the Nearby Star, GJ 876. *Astrophys. J.*, 634, 625-640.
- Saar, S. H., and Donahue, R. A. (1997) Activity-related Radial Velocity Variation in Cool Stars. *Astrophys. J.*, 485, 319-327.
- Saar, S. H., and Fischer, D. (2000) Correcting Radial Velocities for Long-Term Magnetic Activity Variations. *Astrophys. J. Lett.*, 534, L105-L108.
- Santos, N. C., Bouchy, F., Mayor, M., et al. (2004) The HARPS survey for southern extra-solar planets. II. A 14 Earth-masses exoplanet around  $\mu$  Arae. *Astron. Astrophys.*, 426, L19-L23.
- Santos, N. C., Mayor, M., Naef, D., et al. (2000) The CORALIE survey for Southern extra-solar planets. IV. Intrinsic stellar limitations to planet searches with radial-velocity techniques. *Astron. Astrophys.*, 361, 265-272.
- Sato, B., Ando, H., Kambe, E., et al. (2003) A Planetary Companion to the G-Type Giant Star HD 104985. *Astrophys. J. Lett.*, 597, L157-L160.
- Sato, B., Fischer, D. A., Henry, G. W., et al. (2005) The N2K Consortium. II. A Transiting Hot Saturn around HD 149026 with a Large Dense Core. *Astrophys. J.*, 633, 465-473.
- Selsis, F., Kasting, J. F., Levrard, B., et al. (2007) Habitable planets around the star Gliese 581? *Astron. Astrophys.*, 476, 1373-1387.
- Setiawan, J., Hatzes, A. P., von der Lühe, O., et al. (2003) Evidence of a sub-stellar companion around HD 47536. *Astron. Astrophys.*, 398, L19-L23.
- Standish, E. M., Jr. (1990) The observational basis for JPL's DE 200, the planetary ephemerides of the Astronomical Almanac. *Astron. Astrophys.*, 233, 252-271.
- Steinmetz, T., Wilken, T., Araujo-Hauck, C., et al. (2008) Laser Frequency Combs for Astronomical Observations. *Science*, 321, 1335-1337.
- Struve, O. (1952) Proposal for a project of high-precision stellar radial velocity work. *The Observatory*, 72, 199-200.
- Udry, S., Bonfils, X., Delfosse, X., et al. (2007) The HARPS search for southern extra-solar planets. XI. Super-Earths (5 and 8  $M_{\oplus}$ ) in a 3-planet system. *Astron. Astrophys.*, 469, L43-L47.
- Udry, S., Mayor, M., Benz, W., et al. (2006) The HARPS search for southern extra-solar planets. V. A 14 Earth-masses planet orbiting HD 4308. *Astron. Astrophys.*, 447, 361-367.
- Udry, S., and Santos, N. C. (2007) Statistical Properties of Exoplanets. *Ann. Rev. Astron. Astrophys.*, 45, 397-439.
- Valenti, J. A., Butler, R. P., and Marcy, G. W. (1995) Determining Spectrometer Instrumental Profiles Using FTS Reference Spectra. *Publ. Astron. Soc. Pac.*, 107, 966-976.
- Vogt, S. S., Butler, R. P., Marcy, G. W., et al. (2005) Five New Multicomponent Planetary Systems. *Astrophys. J.*, 632, 638-658.
- Walker, G. A. H., Walker, A. R., Irwin, A. W., et al. (1995) A search for Jupiter-mass companions to nearby stars. *Icarus*, 116, 359-375.
- Wilson, O. C. (1978) Chromospheric variations in main-sequence stars. *Astrophys. J.*, 226, 379-396.
- Wilson, R. E. (1953) General Catalogue of Stellar Radial Velocities. *Carnegie Inst. Washington D.C. Publ.*, 601, 1953.
- Wolszczan, A., and Frail, D. A. (1992) A planetary system around the millisecond pulsar PSR1257 + 12. *Nature*, 355, 145-147.
- Wright, J. T. (2005) Radial Velocity Jitter in Stars from the California and Carnegie Planet Search at Keck Observatory. *Publ. Astron. Soc. Pac.*, 117, 657-664.